Anisotropic mechanical characterization of human skin by in vivo multi-axial ring suction test

Aflah Elouneg, Jérôme Chambert, Arnaud Lejeune, Quentin Lucot, Emmanuelle Jacquet, Stéphane Bordas

Anisotropic mechanical characterization of human skin by *in vivo* multi-axial ring suction test

A. Elouneg [a,b], J. Chambert [a], A. Lejeune [a], Q. Lucot [a], E. Jacquet [a], S.P.A. Bordas [a,b,*]

[a] *Université de Franche-Comté, CNRS, institut FEMTO-ST, F-25000 Besançon, France*

[b] *Institute of Computational Engineering and Sciences, Department of Engineering, Université du Luxembourg, Esch-sur-Alzette, Luxembourg*

[*] *Corresponding author: stephane.bordas@uni.lu*

Abstract

Human skin is a soft tissue behaving as an anisotropic material. The anisotropy emerges from the alignment of collagen fibers in the dermis, which causes the skin to exhibit greater stiffness in a certain direction, known as Langer's line. The importance of determining this anisotropy axis lies in assisting surgeons in making incisions that do not produce undesirable scars. In this paper, we introduce an open-source numerical framework, MARSAC (Multi-Axial Ring Suction for Anistotropy Characterization: `https://github.com/aflahelouneg/MARSAC`), adapted to a commercial device CutiScan CS 100® that applies a suction load on an annular section, causing a multi-axial stretch in the central zone, where in-plane displacements are captured by a camera. The presented framework receives inputs from a video file and converts them into displacement fields through Digital Image Correlation (DIC) technique. From the latter and based on an analytical model, the method assesses the anisotropic material parameters of human skin: Langer's line ϕ, and the elastic moduli E_1 and E_2 along the principal axes, providing that the Poisson's ratio is fixed. The pipeline was applied to a public data repository, `https://search-data.ubfc.fr/femto/FR-18008901306731-2021-08-25_In-vivo-skin-anisotropy-dataset-for-a-young-man.html`, containing 30 test series performed on a forearm of a Caucasian subject. As a result, the identified parameter averages, $\hat{\phi} = 40.9 \pm 8.2^\circ$ and the anisotropy ratio $\hat{E}_2/\hat{E}_1 = 3.14 \pm 1.60$, were in accordance with the literature. The intra-subject analysis showed a reliable assessment of ϕ and E_2. As skin anisotropy varies from site to site and from subject to subject, the novelty of the method consists in (i) an optimal utilization of CutiScan CS 100® probe to measure the Langer's line accurately and rapidly on small areas with a minimum diameter of 14 mm, (ii) validation of an analytical model based on deformation ellipticity.

Keywords

Skin Mechanical Characterization, Multi-Axial Extension, Anisotropy, Langer's line, CutiScan® CS 100

1 Introduction

It is essential to study the mechanics of the skin since its behavior under different loads is linked to several skin developments and regeneration dysfunctions in both cellular and tissular scales, including wound healing and scar formation [1, 2]. A thorough *in vivo* analysis of the mechanisms underlying these phenomena combined with clinical trial data may help develop novel therapeutic strategies. The skin, considered a soft tissue, is composed of three primary layers: the epidermis, the dermis, and the hypodermis. Each layer is made of several components. The methodology followed to characterize the mechanical properties of the skin lies in essential steps ordered as follows, measurement, modeling, and parameter identification. There are no general standards for measuring human skin's elasticity *in vivo*. The choice of methods and materials depends on the targeted material parameters and site accessibility. The epidermis, a superficial layer of the skin, has a thickness of approximately 75–150 µm [3] and is composed principally of flattened cells that overlie a base sublayer consisting of columnar cells arranged perpendicularly. The dermis, which has a thickness of 0.87–2.65 mm (combined with the epidermis) [4], is a dense connective tissue consisting of fibrous proteins, collagen, and elastin. Procedures used for *in vivo* testing of the skin include tensile, suction, indentation, and torsion. The mechanical behavior of the dermis, believed to dominate the mechanics of the skin, is dictated by elastin fibers at small strains and stress and by collagen fibers at large strains [5].

The third layer is the hypodermis, a fatty tissue composed mainly of adipose cells. Its thickness varies all over the body and functions as an insulator, constituting about 10% of the body mass [6]. In *in vivo* extension tests, the skin is stretched parallel to its surface. The load can be uni-axial [7–19], bi-axial [20] or multi-axial [21–24]. This experiment quantifies the skin's stiffness and the elastic parameters along the stretched direction(s). Those parameters can also be assessed through other techniques, suction [25–31], indentation [30, 32–36], and torsion [8, 37–39]. The mechanical response of human skin undergoing large deformation exhibits a J-shaped stress-strain curve comprising at least two different regimes. Their respective tangents represent skin stiffness, commonly introduced as the elastic moduli. Their identified values in the earlier cited studies range from 1 kPa to 57 MPa [40–42]. This high variability is due to the choice of the hypotheses involved in developing theoretical models to determine elastic properties. Every model was built to mimic one or many aspects, such as viscoelasticity, hyperelasticity, anisotropy, multi-layer scaling, *etc*. Using a complex model with all the biomechanical aspects is computationally and mathematically challenging [43] and makes the model prone to overfitting.

In the light of recent studies about the mechanical characterization of bi-material keloid-skin [19,44,45], we address the anisotropic characteristics of the healthy skin surrounding the keloid scar. It has been asserted in [46, 47] that during the skin wound healing process, a mechanical stretch field develops in the wound plane. Also, quantitative measurements by laser light scattering showed that the collagen fibers are oriented along the direction of the major contraction vector of the wound rather than quasi-randomly oriented [48]. According to Hendriks [49], the biomechanical properties determined from testing the whole skin are seemingly driven by the dermal collagen [50] since those collagen fibers are the main constituent of the dermis (77% of the fat-free dry weight) running almost parallel with the skin surface [51]. The density distribution of collagen fibers shows a preferential direction of lower extensibility correlated with Langer's lines [52, 53] in numerous studies [54–59]. Therefore, it is vital to identify, *in vivo*, the privileged direction of the collagen bundles in order to prevent the formation of undesired scars after incision [60, 61].

The anisotropy of the skin has been characterized *in vivo* through different non-invasive methods in

the last decades, with optical approaches [62, 63], elastography [64, 65], suction tests [66, 67], and multi-axial tests [13,16,17,22,23,55,68–71]. The latter method is in the form of multiple simple tensile tests carried out in many directions. This method seems to be the most reliable as the deformations are in-plane, corresponding to the alignment of collagen fibers parallel to the dermis layer. However, it has several drawbacks. Conducting multiple tests to obtain a load–extension curve in each direction is time-consuming. Conversely, reducing the number of angles with which the direction of the minimum extensibility can be defined will affect the accuracy [72].

A novel technique was recently used to investigate the anisotropy of soft tissue in all directions simultaneously, continuously, and locally. By applying a suction load within an annular surface, the central zone is subjected to multi-axial stretch. The preferential direction of collagen fibers is precisely quantified from the resulting full-field displacements. For that purpose, Laiacona *et al*. [24] have developed a home-made device with negative pressure of 170 mbar and inner and outer diameters, respectively, 30 mm and 49 mm. A commercial device CutiScan® CS 100[1], utilized in [73–78], has been introduced in the market by Courage + Khazaka electronic GmbH, with an inner diameter of 5 mm (respectively outer diameter of 14 mm), granting measurement of multi-axial stretch on a small region, such as the earlobe [77].

Although the CutiScan device is reliable and promising [78], its original software has some limitations, as reported in [77]. Indeed, the angle of the minimum displacement (equivalent to Langer's line) is given in the associated software, but access to the data of the displacement full-field is not provided. Furthermore, the anisotropy axis is hard to estimate as the displacement field shows a symmetry axis barely. And the displacement values given in pixels are multiplied by an unknown factor, which makes it unable to convert the displacements into millimeters to assess the strains. Thus, we had the motivation to adapt the Device's output treatment according to our research context and popularize it through this article.

In this work, we present an open-source methodology to identify the privileged direction of collagen fibers in the skin from a multi-axial ring suction test performed by the CutiScan® CS 100 probe. The displacement fields are computed *via* the DIC technique starting from a video file recorded by the commercial device and divided into frames. From a field matching the quasi-static configuration, displacement data are gathered on a specific circle and fitted with an analytical orthotropic linear model. The anisotropy direction and the elastic material parameters are identified through an optimization method. We present the application of this numerical pipeline[2] on a latex material and the forearm of a 28-years-old Caucasian volunteer, whose public dataset [3] was described in the data paper [79]. The reader can refer to the repository `https://figshare.com/s/0f3612238200cc98fb27` [80] to reproduce the results of the paper.

[1] `https://www.courage-khazaka.de/en/scientific-products/efficacy-tests/skin?view=article&id=179&catid=16`

[2] `https://github.com/aflahelouneg/MARSAC/`

[3] `http://dx.doi.org/doi:10.25666/DATAOSU-2021-08-25`

2 Material and methods

2.1 Experiments

2.1.1 Multi-axial ring suction test

The *in vivo* experimental design used to characterize the anisotropic behavior of human skin in the present study is built around the commercial apparatus CutiScan® CS 100 (referenced CutiScan® thereafter), developed by Courage + Khazaka electronic GmbH. It comprises two main parts (Fig. 1): a suction probe and a central device. The probe is equipped with a black-and-white CCD camera (charge-coupled device), including UV light (Fig. 2a). It applies a constant negative pressure p within an annular ring area (inner diameter 5 mm and outer diameter 14 mm) to draw a uniformly soft layer for a predefined phase t_{creep} (Fig. 2b). A double-sided adhesive prevents sliding between the probe and the skin surface. Then, the pressure is completely and instantaneously released during another phase t_{relax}. For the whole creep-relaxation cycle, the in-plane displacement of the material studied is recorded with a µEye® camera inside a zone of interest (ZOI) of 5 mm diameter.

Figure 1: CutiScan® CS 100.

The negative pressure is supplied from the central device, where the vacuum pump is installed. The user can set the nominal pressure $p \in [100; 500]$ mbar, suction time $t_{\text{creep}} \in [1; 3]$ s, relaxation time $t_{\text{relax}} \in [1; 3]$ s, and $t_{\text{standby}} \in [1; 10]$ s. The latter is the waiting time between a pre-cycle and the principal recorded cycle. The pre-cycle can be skipped if unnecessary deformations are not desired (soft materials may take longer to recover their initial configuration due to viscous effects). However, we recommend maintaining the pre-cycle to regulate brightness inside the probe. To minimize unnecessary tensions, we set $t_{\text{creep}} = 1$ s and $t_{\text{relax}} = 1$ s in the pre-cycle, then $t_{\text{standby}} = 10$ s. Whilst in the principal cycle, $t_{\text{creep}} = 3$ s, and $t_{\text{relax}} = 3$ s.

2.1.2 Displacement field measurement

A closed-source framework is provided with the device to convert the videos into steady displacement plots for every 360 angle through the DIC. However, the exact position of the point where the displacement-time curve is built is unknown, and the user has no access to the full-field data. To overcome this limitation, an open-source Python-based program, PyDIC [81], has been adapted (`https://github.com/aflahelouneg/MARSAC/blob/main/pydic.py`) to split the recorded

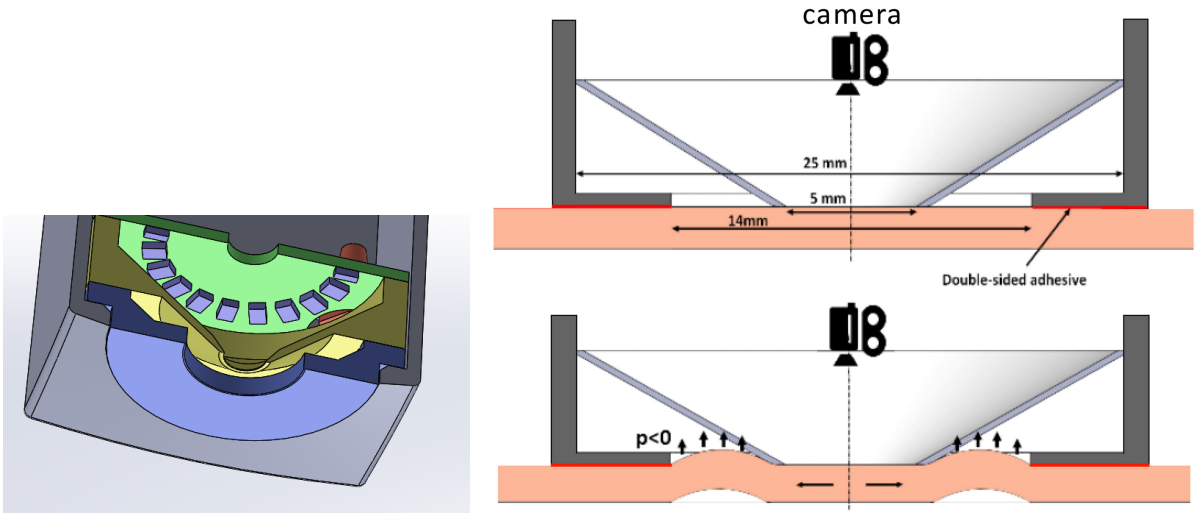

(a) (b)

Figure 2: (a) A cross-sectional view through a CAD model of the probe. The suction fits the circular opening between the blue plastic part and the yellow aluminum reflector. The UV light is emitted from the purple rectangles distributed around the camera lens in the center. Permission was granted from Courage + Khazaka GmbH to publish the drawing. (b) Suction probe cross-section [77]. The aspiration uniformly applied between the cone and the wall results in a multi-axial extension of the soft layer.

video extracted from the commercial software into frames and compute the displacement vectors at the mapped nodes. The Lucas-Kanade method was employed to track motions [82]. The DIC technique in this framework is implemented based on `OpenCV` (Computer Vision), a graphic open-source Python library [83]. On the basis of a calibration study, the correlation parameters, grid resolution, and correlation window size were fixed to be 20 pixels and 40 pixels, respectively. The coordinate grid is mapped with 49×49 nodes (Fig. 3).

2.1.3 Reference material

The validation of the method was carried out on the basis of a calibration study, where we checked the presented method's ability to characterize the soft materials reliably. Thus, a thin homogeneous layer of rubber latex of 220-µm thickness was subjected a the multi-axial ring suction test at constant pressure $p = 300$ mbar. From the recorded video of 6 s, 81 frames were extracted and converted into displacement fields. We retained only the frame corresponding to the quasi-static configuration at the end of the creep phase (around 3 s). The output displacement field was expected to be purely radial. In a parallel experiment, by means of the uni-axial tensile test, 3 rectangular samples of the same latex tissue were cut out along the directions $0\,^\circ$, $45\,^\circ$, and $90\,^\circ$. By calculating the initial tangent of the stress-stretch curve, one may obtain the elastic modulus $E_{\text{latex}} = 2.7 \pm 0.42$ MPa. The results from the multi-axial and uni-axial experiments were combined to calibrate a linear orthotropic elastic model in Section 3.2.1.

2.1.4 Subject forearm test

30 series of multi-axial ring suction tests were conducted on the volar left forearm of a 28-years-old Caucasian male (Fig. 5), following the principles outlined in the Helsinki Declaration of 1975, as revised

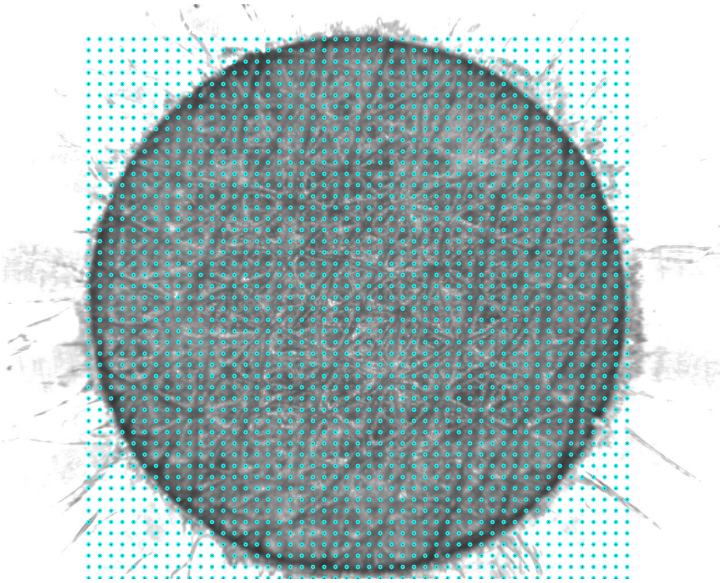

Figure 3: DIC coordinate grid in the initial configuration.

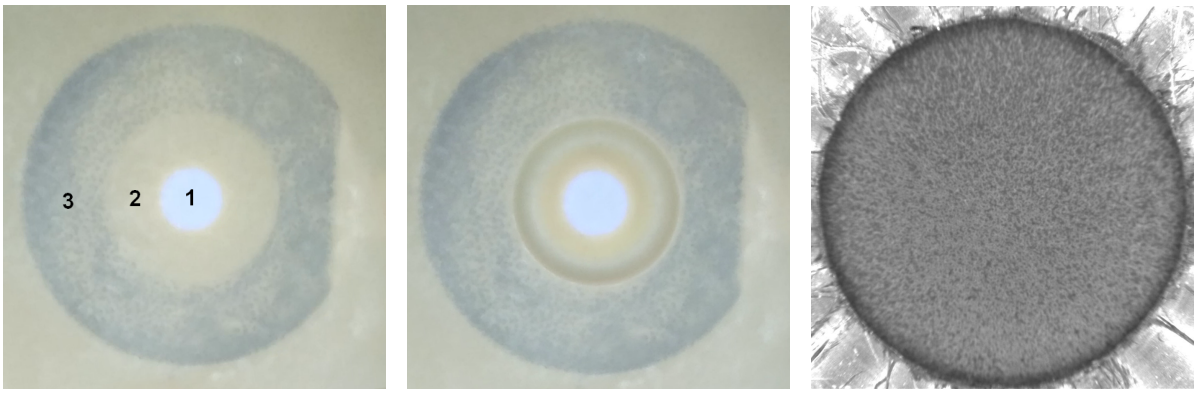

(a) Initial configuration **(b)** Deformed configuration **(c)** Observable zone

Figure 4: Ring suction operation performed on a latex tissue: **(a)** Bottom view before loading; **(b)** Bottom view after loading; **(c)** Top view of the observable zone obtained by the camera before loading. In the central observable zone (1), the UV camera captures the displacement of the stretched layer subjected to suction applied to the annular zone (2). A double-sided annular sticker was settled on the annular zone (3).

in 2000. The site has been chosen for its flatness and easy access. The measured area is located at a distance of 15 cm from the wrist. The epidermis-dermis layer has a thickness of $th_{\mathrm{h}} = 1.47$ mm and was quantified by ultrasound echography. A single series consists of 21 cycles with pressure set-point values varying from 100 mbar to 500 mbar with a step of 20 mbar. A delay of 2 minutes was arbitrarily set between each complete suction cycle by considering that a weak load has a non-significant impact on skin conditioning. It is a common practice in dermatology that a waiting period between successive loadings is brief. In Takema et al.'s study [84], the relaxation period was 2 seconds for 3 pressure levels, 200, 300, and 400 mbar, with a Cutometer device. In addition, the CutiScan® applies a pre-load cycle of 10 s before each recordable load cycle, making the influence of the delay period less significant.

The video files recorded with CutiScan® software were stored as primary data in a public repository `https://search-data.ubfc.fr/femto/FR-18008901306731-2021-08-25_In-vivo-skin-anisotropy-dataset-for-a-young-man.html`, and from which displacement fields were computed as secondary data using our numerical DIC tool. The latter is available in the same repository, as well as Python codes used to generate them (for more technical details about the experiment, see data paper [79]).

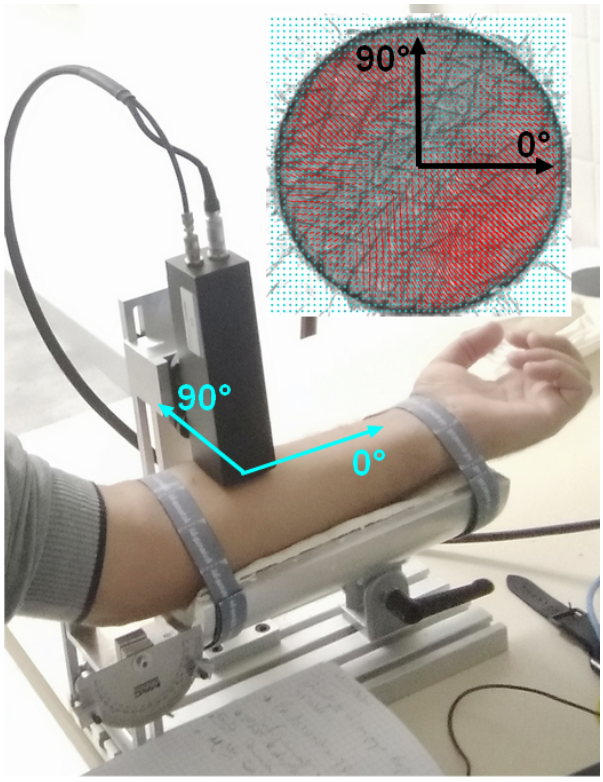

Figure 5: Experimental set-up of the ring suction test performed on the volar forearm and illustration of displacement field vectors. *Source:* Obtained by DIC method [79].

As the present study focuses on the characterization of the anisotropy in healthy skin independently of viscoelastic effects, a data pre-selection was done. The displacement field resulting from the frame captured at the quasi-static state was selected for a pressure $p = 300$ mbar. According to the observations, the results are more reproducible at that pressure level. The mean displacement over 30 tests is then computed at every node of the DIC coordinate grid. As a result, the mean-displacement field will be used as one set of data for the primary analysis.

2.2 Modeling

2.2.1 Problem description

The annular suction test can be modeled as a simplified 2D problem with Neumann boundary conditions characterized by radial traction force $\boldsymbol{t}$ applied to the external frontier and locking conditions (or zero displacements) at the center of the domain to avoid rigid body displacements (Fig. 6a). The Cartesian basis $\{\boldsymbol{e}_1, \boldsymbol{e}_2\}$ (with Cartesian coordinates x_1 and x_2) on which the model is built is not to be confused with the basis $\{\boldsymbol{e}'_1, \boldsymbol{e}'_2\}$ used for the experimental displacement fields. They differ by an angle $\phi = (\boldsymbol{e}'_1, \boldsymbol{e}_1)$, representing the orientation of the Langer's line (Fig. 7).

We assume in our approach that:

- The considered problem can be treated by plane stress conditions in the (x_1, x_2) plane.
- The friction effects between the skin and CutiScan® probe are not considered (Fig. 2b).
- A uniform in-plane radial stress σ_r taking place over all the observable zone is linearly correlated with the supplied negative pressure.
- The skin within the observable zone is subjected to small strains and behaves as a linear orthotropic material.

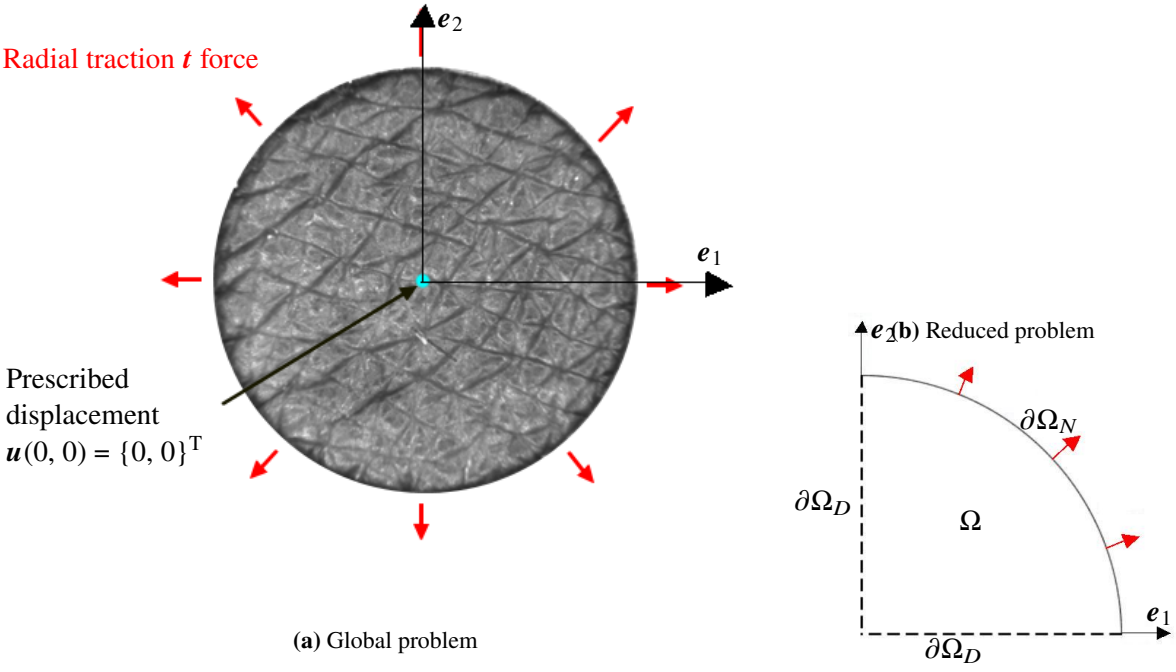

Figure 6: Boundary conditions of the global (a) and reduced (b) problems.

Consider the deformable body occupying a disk corresponding to the observable zone defined by CutiScan® (Fig. 6a). Knowing that the axes $(x_1 = 0)$ and $(x_2 = 0)$ are symmetry axes from geometrical and material points of view, only a quarter of the problem is taken into account. The external boundary $\partial\Omega$ of the domain Ω (a quarter of disk) can be split into a Dirichlet part $\partial\Omega_{\mathrm{D}}$ and a Neumann part $\partial\Omega_{\mathrm{N}}$ such as $\partial\Omega = \partial\Omega_{\mathrm{D}} \cup \partial\Omega_{\mathrm{N}}$ and $\partial\Omega_{\mathrm{D}} \cap \partial\Omega_{\mathrm{N}} = \emptyset$ (Fig. 6b).

Similarly, as in [85], the local formulation of the static problem consists in finding the tensor fields of displacements $\boldsymbol{u}$, strains $\boldsymbol{\varepsilon}$ and stresses $\boldsymbol{\sigma}$ which satisfy the following equations:

$$\begin{aligned}
&\boldsymbol{\nabla} \cdot \boldsymbol{\sigma} = \mathbf{0} \quad \text{in } \Omega \\
&\boldsymbol{\sigma} \cdot \boldsymbol{n} = \sigma_r \, \boldsymbol{n} \quad \text{on } \partial\Omega_{\mathrm{N}} \\
&u_1(0, x_2) = 0 \quad \text{and} \quad u_2(x_1, 0) = 0 \quad \text{on } \partial\Omega_{\mathrm{D}} \\
&\boldsymbol{\varepsilon} = \frac{1}{2}\left(\boldsymbol{\nabla}\boldsymbol{u} + \boldsymbol{\nabla}^{\mathsf{T}}\boldsymbol{u}\right) \\
&\boldsymbol{\sigma} = \mathbf{C} : \boldsymbol{\varepsilon}
\end{aligned} \tag{1}$$

In the absence of body forces, Eq. (1a) stands for the equilibrium equations within the deformable domain Ω. Eq. (1b) represents the Neumann boundary conditions with $\boldsymbol{n}$ the normal vector to the external boundary domain $\partial\Omega_{\mathrm{N}}$. σ_r is the radial stress resulted from the applied $\boldsymbol{t}$. Eq. (1c) describes the Dirichlet boundary conditions. Eq. (1d) represents the infinitesimal strain-displacement relations. Eq. (1e) constitutes the stress-strain equations where $\mathbf{C}$ is the fourth-order tensor, also called the elasticity operator. In matrix form, Eq. (1e) for an orthotropic linear elastic material under plane-stress conditions [86] is given by:

$$\begin{Bmatrix} \sigma_{11} \\ \sigma_{22} \\ \sigma_{12} \end{Bmatrix} = \frac{1}{1 - \nu_{12}\nu_{21}} \begin{bmatrix} E_1 & \nu_{21}E_1 & 0 \\ \nu_{12}E_2 & E_2 & 0 \\ 0 & 0 & (1 - \nu_{12}\nu_{21})G_{12} \end{bmatrix} \begin{Bmatrix} \varepsilon_{11} \\ \varepsilon_{22} \\ 2\varepsilon_{12} \end{Bmatrix} \tag{2}$$

where σ_{11}, σ_{22} and σ_{12} (respectively, ε_{11}, ε_{22} and ε_{12}) are the components of the stress tensor $\boldsymbol{\sigma}$ (respectively, the strain tensor $\boldsymbol{\varepsilon}$). E_1 and E_2 are the Young's moduli, G_{12} is the shear modulus, and ν_{12} and ν_{21} are the Poisson's ratios. In the observable zone, the in-plane radial stress is presupposed to be uniform, as $\sigma_{11} = \sigma_{22} = \sigma_r$.

For symmetry conditions on stiffness and compliance matrices, we get:

$$\frac{\nu_{12}}{E_1} = \frac{\nu_{21}}{E_2} \tag{3}$$

Consequently, only 4 material parameters are independent: E_1, E_2, G_{12}, and ν_{12}.

2.2.2 Analytical model

As Fig. 7 shows, the initial circular domain transforms into an elliptical deformed shape due to multiaxial loading and orthotropic behavior. Accordingly, we assume the following analytical form for the Cartesian displacement field:

$$\begin{cases} u_1(r, \theta) = A_1 r \cos\theta \\ u_2(r, \theta) = A_2 r \sin\theta \end{cases} \quad ; \quad r \in [0, R] \quad ; \quad \theta \in [0, 360^\circ] \, , \tag{4}$$

where r and θ are the cylindrical coordinates defined by $r = \|\overrightarrow{OM}\|$ and $\theta = (\boldsymbol{e}_1, \overrightarrow{OM})$, in which $\overrightarrow{OM}$ is the position vector of a material point in the Cartesian system $\{O; \boldsymbol{e}_1, \boldsymbol{e}_2\}$. The radius R corresponds to the frontier of the observable zone. A_1 and A_2 are constants.

From the infinitesimal strain-displacement relations (1d) and the constitutive equations of orthotropic

linear elasticity (2), we obtain uniform strain and stress fields. Consequently, the equilibrium equations (1a) are always satisfied. Using Neumann boundary conditions (1b) and after computations, we express A_1 and A_2 as:

$$\begin{cases} A_1 = \dfrac{\sigma_r(1-\nu_{12})}{E_1} \\ A_2 = \dfrac{\sigma_r(1-\nu_{21})}{E_2} \end{cases} \tag{5}$$

Finally, the analytical solution for the Cartesian displacement field in terms of Cartesian coordinates x_1 and x_2 is given by:

$$\begin{cases} u_1(x_1) = \dfrac{\sigma_r(1-\nu_{12})}{E_1} x_1 \\ u_2(x_2) = \dfrac{\sigma_r(1-\nu_{21})}{E_2} x_2 \end{cases} \tag{6}$$

2.2.3 FEM model

Subjected to the Dirichlet and Neumann conditions (Fig. 6), the problem can be easily written in a weak form over skin domain Ω (observable disk-zone) with boundary $\partial\Omega$, and solved with Finite Element Method (FEM) by using FEniCS software/framework [87]. In the absence of body force, its weak formulation writes:

$$\text{Find } \boldsymbol{u} \in \mathcal{U} \text{ such that } \forall \boldsymbol{v} \in \mathcal{V}_0, \ \int_\Omega \boldsymbol{\sigma}(\boldsymbol{u}) : \boldsymbol{\nabla}^{\text{sym}} \boldsymbol{v} \, \mathrm{d}\Omega = \int_{\partial\Omega} (p\boldsymbol{n}) \cdot \boldsymbol{v} \, \mathrm{d}\Gamma \tag{7}$$

Assuming $\mathcal{U}$, a space of sufficiently smooth functions and $\mathcal{V}_0$, its counterpart satisfying homogeneous boundary condition on the Dirichlet boundary $\partial\Omega_{\text{D}}$. The domain Ω, taking the shape of a quarter of a disk, is meshed into quadratic triangular finite elements, and the size of each element is approximately equal to 50 µm (55174 degrees of freedom).

2.3 Methodology for material parameters characterization

In the case of 2D orthotropic linear elastic material under plane-stress conditions, we present in this section a determination methodology for the material parameters of the skin by using CutiScan® apparatus: Poisson's ratio ν_{12}, shear modulus G_{12}, and Young's moduli E_1 & E_2.

2.3.1 Determination of Poisson's ratio and shear modulus

CutiScan® apparatus imposes a hydrostatic stress state with in-plane pressure p set at the boundary of the observable zone. This loading implies a multi-axial stretch that does not allow to identify the Poisson's ratio ν_{12} (or ν_{21}) for skin orthotropic material. Indeed, Ting and Chen [88] have shown that Poisson's ratio for anisotropic materials can have no theoretical bounds. Though, it had been fixed arbitrarily for human skin between 0.3 and 0.5 because of its rubber-like mechanical properties [13, 40, 89, 90]. Destrade *et al.* [91] pointed out that the usual practice of arbitrarily choosing a value of Poisson's ratio when numerically modeling rubbers and soft tissue will, almost certainly, lead to a significant difference between the simulated and actual normal stresses in a sheared block. Moreover, the collagen fiber

orientation affects Poisson's ratio variation [92]. The modeler would need a robust hypothesis to associate the classical Poisson's ratio with the parameter ν_{12}. Hence, based on an multi-axial study conducted by Reihsner *et al.* [22], we define: $\nu_{12} = C_{12}/C_{22} = 0.43 \pm 0.09$ with $C_{12} = \frac{\nu_{12}E_2}{1-\nu_{12}\nu_{21}} = 4.0 \pm 0.6$ Nm/g and $C_{22} = \frac{E_2}{1-\nu_{12}\nu_{21}} = 9.4 \pm 1.4$ Nm/g are elastic coefficient determined by the experiment on 16 sites of a 30-years-old subject skin [22]. Considering that no shear strain and no shear stress are activated by CutiScan® loading within the skin observable zone, the shear modulus G_{12} can be arbitrarily chosen: thereafter, $G_{12} = 1$ MPa.

2.3.2 Identification of geometrical parameters and Young's moduli

The strategy adopted to identify the material parameters consists of two steps.

First, by means of the non-linear Newton-Raphson method, the geometrical parameters $\boldsymbol{m}_g = \{a, b, \phi\}$ are calibrated from the elliptic deformation configuration associated with a circle with radius r in the undeformed state (Fig. 7).

$$\begin{cases} \hat{x}_1(r,\theta) = a(r)\cos\theta \\ \hat{x}_2(r,\theta) = b(r)\sin\theta \end{cases} \quad ; \quad r \in [0, R] \quad ; \quad \theta \in [0, 360^\circ] \tag{8}$$

Second, the material parameters $\boldsymbol{m}_m = \{E_1, E_2\}$ are derived from the principal minor and major semi-axes of the ellipse, respectively, a and b, *via* the model as

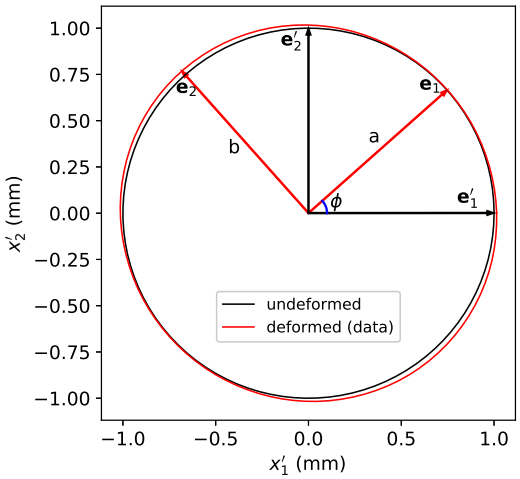

Figure 7: Initial and deformed configurations for $r = 1$ mm. $\{\boldsymbol{e}_1', \boldsymbol{e}_2'\}$ coordinate system corresponds to the probe referential (with $\boldsymbol{e}_1'$ oriented along the forearm toward the hand). The model is expressed in the system $\{\boldsymbol{e}_1, \boldsymbol{e}_2\}$ to fit the targeted data.

$$\begin{cases} a(r) = r + u_1(r) = r\left(1 + \dfrac{\sigma_r(1-\nu_{12})}{E1}\right) \\ b(r) = r + u_2(r) = r\left(1 + \dfrac{\sigma_r(1-\nu_{12}E_2/E_1)}{E2}\right) \end{cases} \tag{9}$$

The material parameters can be assessed from Eqs. (6) and (9) given r as

$$\begin{cases} E_1(r) = \dfrac{\sigma_r(1-\nu_{12})r}{a-r} \\ E_2(r) = \dfrac{\sigma_r(1-\nu_{12})r}{b(1-\nu_{12})+\nu_{12}a-r} \end{cases} \tag{10}$$

The inverse identification of the geometrical parameter set $\boldsymbol{m}_g$ is processed according to a least-squares non-linear optimization method. By a similar method as in [36], the error function on one point $\{x_1{}'_k, x_2{}'_k\}^{\mathrm{T}}$ is the mismatch of ellipses radii between the model – in the rotating system – and the data from [79]. The optimization problem considers the rigid body motion, which is assessed by identifying the coordinates x_{10} and x_{20} of the center after deformation. Hence, the total parameter set to be estimated is $\tilde{\boldsymbol{m}}_g = \boldsymbol{m}_g \cup \{x_{10}, x_{20}\}$. The objective function reads

$$J_k(r, \theta_k, \tilde{\boldsymbol{m}}_g) = \frac{1}{2}\left[\sqrt{\left(\hat{x}_1^{\mathrm{R}}(r,\theta_k,a,b,\phi) - x_{10}\right)^2 + \left(\hat{x}_2^{\mathrm{R}}(r,\theta_k,a,b,\phi) - x_{20}\right)^2} - \sqrt{{x_1{}'_k}^2 + {x_2{}'_k}^2}\right]^2 \tag{11}$$

such that $\theta_k = \arctan(x_2{}'_k / x_1{}'_k)$. $\hat{x}_1^{\mathrm{R}}$, and $\hat{x}_2^{\mathrm{R}}$ (see Eq. (12)) result from the rotation of $\{\boldsymbol{e}_1, \boldsymbol{e}_2\}$ with respect to $\{\boldsymbol{e}'_1, \boldsymbol{e}'_2\}$ by the angle ϕ (Fig. 7).

$$\begin{cases} \hat{x}_1^{\mathrm{R}}(r,\theta,a,b,\phi) = a(r)\cos(\theta-\phi)\cos\phi - b(r)\sin(\theta-\phi)\sin\phi \\ \hat{x}_2^{\mathrm{R}}(r,\theta,a,b,\phi) = a(r)\cos(\theta-\phi)\sin\phi + b(r)\sin(\theta-\phi)\cos\phi \end{cases} \tag{12}$$

Since the displacement vectors are independent of each other, the total error function for each ellipse $J(r)$ is quantified for all N_k chosen nodes as

$$J(r, \tilde{\boldsymbol{m}}_g) = \sum_{k=1}^{N_k} J_k(r, \theta_k, \tilde{\boldsymbol{m}}_g) \tag{13}$$

Starting from an initial guess $\tilde{\boldsymbol{m}}_g^{(0)}$, we compute iteratively the change on the parameters $\delta\tilde{\boldsymbol{m}}_g$ by way of the Newton-Raphson method (see Eq. (14)) until reaching the absolute convergence criteria of 10^{-9} on every parameter. The detailed expression of the Gradient vector $\frac{\partial J}{\partial \tilde{\boldsymbol{m}}_g}$ and the symmetrical Hessian matrix $\frac{\partial^2 J}{\partial \tilde{\boldsymbol{m}}_g^2}$ can be found in the framework code `https://github.com/aflahelouneg/MARSAC/blob/main/newton.py`.

$$\tilde{\boldsymbol{m}}_g^{(n+1)} = \tilde{\boldsymbol{m}}_g^{(n)} - \left[\frac{\partial^2 J}{\partial \tilde{\boldsymbol{m}}_g^2}\right]^{-1} \cdot \left[\frac{\partial J}{\partial \tilde{\boldsymbol{m}}_g}\right] \tag{14}$$

2.4 Statistical analysis

The interquartile range method was used in this study to discard the outlier values among the results of 30 tests. Therefore, 12 values were removed for E_1, 4 values for E_2, and 3 values for ϕ. We denote $\hat{E}_1$, $\hat{E}_2$, and $\hat{\phi}$, the average values over the tests of E_1, E_2, and ϕ, respectively. The global uncertainty of $\hat{E}_j$ ($j = \{1, 2\}$) takes into account the day-to-day variation of mechanical response and $\Delta_{\nu_{12}}$ (uncertainty of

ν_{12}). They were computed according to the weighted standard deviation method.

$$\begin{aligned} \bar{E}_j &= \frac{\sum_i^{n_j} w_i E_j^{(i)}}{\sum_i^{n_j} w_i} \\ \bar{\Delta}_{E_j} &= \sqrt{\frac{\sum_i^{n_j} w_i (E_j^{(i)} - \bar{E}_j)^2}{(n_j - 1)\frac{\sum_i^{n_j} w_i}{n_j}}} \end{aligned} \tag{15}$$

with n_j the number of admissible values within the interquartile range, and the weights $w_i = 1/\Delta_{E_j}^{(i)^2}$, such that $\Delta_{E_j}^{(i)}$ is the uncertainty of $E_j^{(i)}$ for each test i. Therefore, $\hat{E}_j = \bar{E}_j \pm \bar{\Delta}_{E_j}$

3 Results

3.1 FEM versus analytical model

The solution of the linear elastic problem defined by Eq. (1) was computed by FEM, and the analytical model with ranges of material parameter set coming from skin's literature ([8, 10–14, 17, 19, 41]). For different orders of E_1-magnitude, $E_1 = \{0.01, 0.1, 1, 10\}$ MPa, we set the following ranges: $E_1/E_2 = \{1, 2, \ldots, 19, 20\}$, $\nu_{12} = \{0, 0.05, \ldots, 0.90, 0.95\}$ and $G_{12} = 1$ MPa. Thus, $(4E_1) \times (20E_2) \times (20\nu_{12}) = 1600$ FE simulations were performed. The minimum and maximum absolute errors between FEM and analytical solutions evaluated on nodes are 2.81×10^{-6} and 3.0×10^{-15}, respectively. For the arbitrary choice of parameter set ($E_1 = 10$ kPa, $E_2 = 0.5$ kPa, $\nu_{12} = 0.5$, $G_{12} = 1$ MPa), the displacement vector fields for analytical ($\boldsymbol{u}$) and FEM ($\boldsymbol{u}_{\text{FEM}}$) models have been carried out along circles $r = \{0.5, 1.0, 1.5, 2.0, 2.5\}$ mm in Fig. 8. A full-field displacement map obtained by FEM is presented in Fig. 9 for the same parameter set.

3.2 Material characterization

3.2.1 Calibration study

The presented method was validated based on two significant features: radial displacement and stiffness. As the radial in-plane stress σ_r is uniform, the anisotropy is due only to the directional variation of the stiffness. Thus, using an isotropic latex material for validation of an orthotropic model (Eq. (6)) is plausible for the condition $E_1 = E_2$. The data acquired from the experiments are described in Section 2.1.3.

Firstly, we check that the deformation of the reference material captured by the camera is radially regular. In Fig. 10, we plotted the mechanical response of the latex material in the quasi-static state. It consists of a displacement field captured by DIC and the deformation of the circle with 1 mm radius in the undeformed state. By using the linear interpolation all over the grid (provided by `SciPy` library), the values of the radial component of the displacements (u_r) were computed and displayed in Fig. 11 as a form of contour lines, as well as along the radial lines with the respective orientations $\{0°; 45°; 90°; 135°\}$.

Starting from an initial guess corresponding to an anisotropic situation $\tilde{\boldsymbol{m}}_g^{(0)} = \{a = 1.0 \text{ mm}; b = 1.1 \text{ mm}; \phi = 0°; x_{10} = 0 \text{ mm}; x_{20} = 0 \text{ mm}\}$ and by choosing $N_k = 100$, the inverse identification performed on each test data over the circle ($r = 1$ mm) results in the following converging parameter set

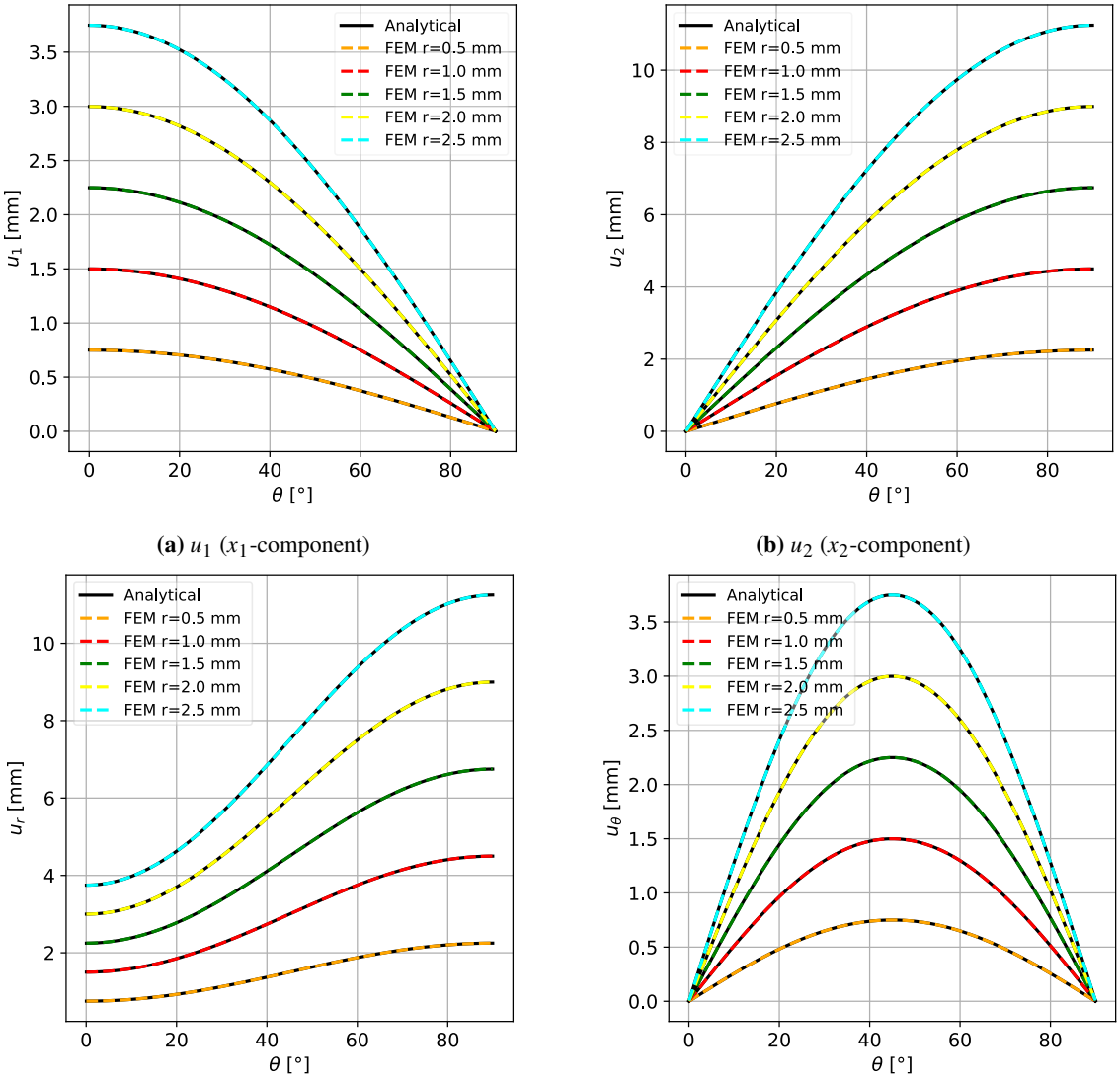

(a) u_1 (x_1-component)

(b) u_2 (x_2-component)

(c) u_r (radial component)

(d) u_θ (ortho-radial component)

Figure 8: Components of analytical and FEM displacement vector fields on circles with various radius r for the parameter set ($E_1 = 10$ kPa, $E_2 = 0.5$ kPa, $\nu_{12} = 0.5$, $G_{12} = 1$ MPa).

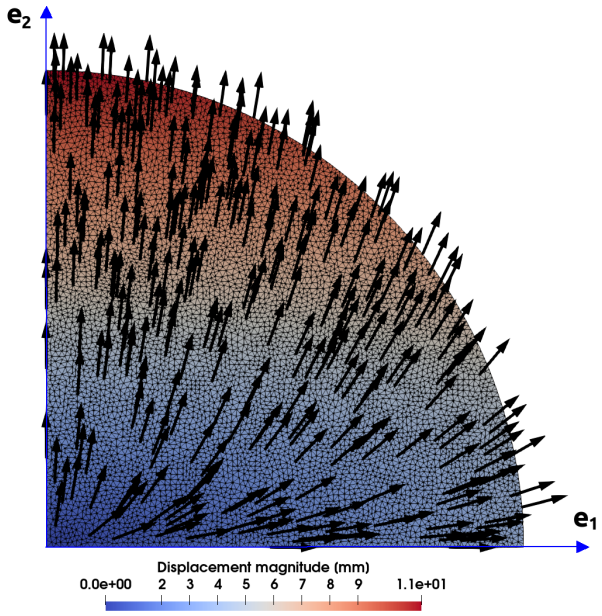

Figure 9: Displacement vector field $\boldsymbol{u}_{\mathrm{FEM}}$ for the parameter set ($E_1 = 10$ kPa, $E_2 = 0.5$ kPa, $\nu_{12} = 0.5$, $G_{12} = 1$ MPa). The norm $\|\boldsymbol{u}_{\mathrm{FEM}}\|$ is given by the color bar. The directions of the vector field $\boldsymbol{u}_{\mathrm{FEM}}$ are represented by arrows without taking into account the magnitude scale.

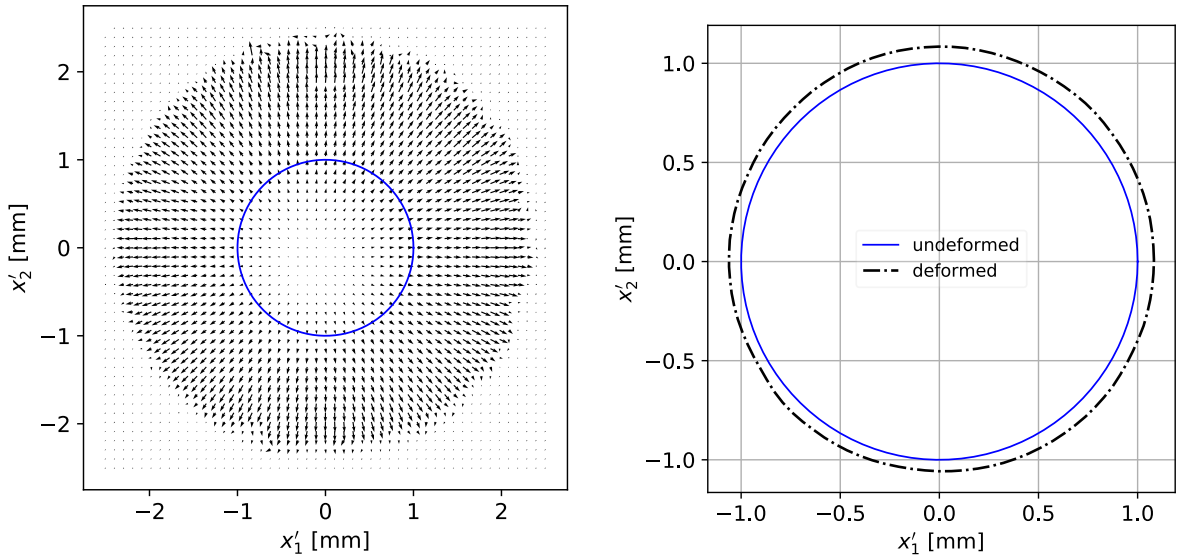

(a) Displacement vector field

(b) Deformation of the circle ($r = 1$ mm)

Figure 10: Mechanical response of the latex material under multi-axial ring suction load.

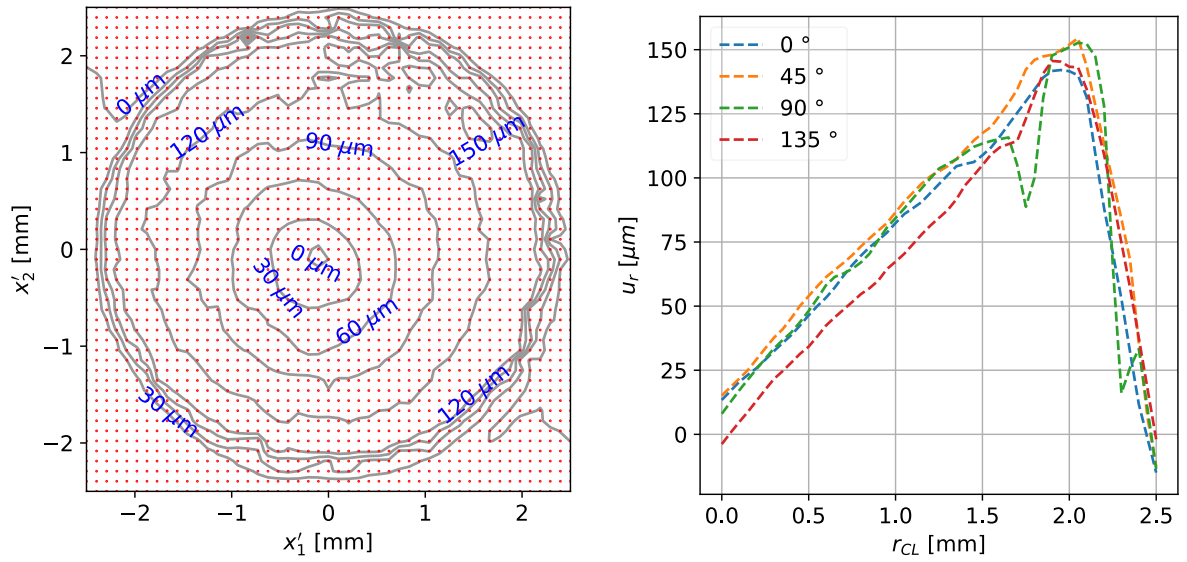

(a) Contour lines of u_r-component

(b) Radial cutlines

Figure 11: Radial displacement component of the latex material under multi-axial ring suction load. Data on circles and cutlines are extracted from the displacement field.

(I, II, and III, stand for 3 tests, respectively) $\tilde{\boldsymbol{m}}_g^{\mathrm{I}} = \{a = 1.0708 \text{ mm}; b = 1.071 \text{ mm}; \phi = -0.67°; x_{10} = -11.2 \text{ µm}; x_{20} = -9.8 \text{ µm}\}$ with coefficient of correlation $R_{\mathrm{cor}} = 0.973$. The model fitting is represented in Fig. 12. Results from 2 similar test conducted in the same conditions are $\tilde{\boldsymbol{m}}_g^{\mathrm{II}} = \{a = 1.0706 \text{ mm}; b = 1.0722 \text{ mm}; \phi = -17.97°; x_{10} = -11.7 \text{ µm}; x_{20} = -12.1 \text{ µm}\}$ ($R_{\mathrm{cor}} = 0.9813$) and $\tilde{\boldsymbol{m}}_g^{\mathrm{III}} = \{a = 1.0718 \text{ mm}; b = 1.0727 \text{ mm}; \phi = -34.53°; x_{10} = -10.8 \text{ µm}; x_{20} = -11.0 \text{ µm}\}$ ($R_{\mathrm{cor}} = 0.9753$). Consequently, the ratio u_1/u_2 used to quantify the isotropicity of the latex material over the 3 tests is 0.9875 ± 0.0097, whereas the uncertainty on the captured displacement was evaluated to be $\Delta_{\mathrm{exp}} = 2.7$ µm.

Secondly, we investigate the correlation between the applied pressure on the annular section and the radial stress in the observable zone. This study was performed on the basis of a frictionless contact-based 2D axisymmetric simulation model built in COMSOL Multiphysics® software (Fig. 13a). The details about the mesh and the boundary conditions are reported in Appendix A.1. Before exploiting the model to establish a link between p and $\tilde{\sigma_r}$, we validate it using the data of the first multi-axial test conducted on the latex material, whose elastic modulus is $E_{\mathrm{latex}} = 2.7 \pm 0.42$ MPa. $\tilde{\sigma}_r$ represents the radial stress in the 2D axisymmetric FE model, while σ_r is associated with the analytical plane model (Eq. (6)). A corrective coefficient η is used to guarantee that the elastic moduli in both models are equivalent. Thus, $\sigma_r = \eta\tilde{\sigma}_r$. To simulate incompressibility, the Poisson's ratio was set to $\nu_{\mathrm{latex}} = 0.495$. Once the rigid body motion was removed, the displacement of the latex was confronted against the simulation in Fig. 13b.

The simulation was run for different values of pressure $p \in \{50, 100, 150, 200, 250, 300\}$ mbar, where $\tilde{\sigma}_r$ was evaluated on the top surface, for each step. Fig. 14 exhibits a linear correlation between p and $\tilde{\sigma_r}$ with a correlation coefficient $R_{\mathrm{cor}} = 0.995$ and a slope of $\xi = 633$. Consequently, we can establish the function $\sigma_r(p) = \eta p/\xi$ to assess the radial stress for any applied pressure between 0 and 300 mbar at least. Given the stress value $\tilde{\sigma}_r = 0.47$ MPa (corresponding to $p = 300$ mbar), the measured displacements along one principal axis $a - r = 71$ µm, and $\eta = 0.81$, the elastic modulus was evaluated

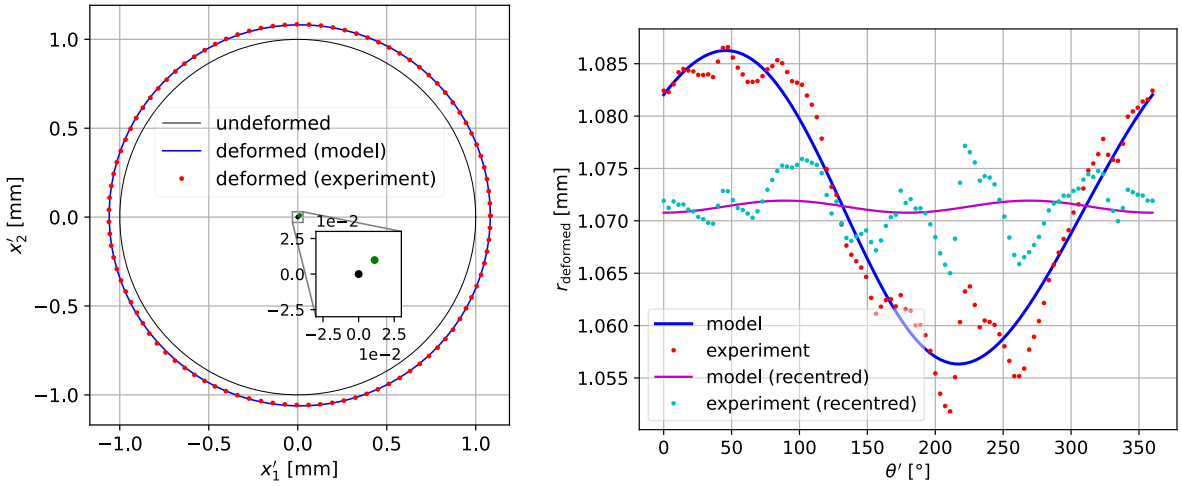

(a) **(b)**

Figure 12: (a) Model fitting with the identified parameters of the latex material $\boldsymbol{m}_g^{\mathrm{I}}$. The center position shifted from the black to the green dot. (b) Radius change r_{deformed} of the deformed ellipse before and after removing the rigid body motion (recentring). r_{deformed} equals to $r + u_r$, with u_r the radial component of the displacement vector. $\theta' = (\boldsymbol{e}_1', \overrightarrow{OM})$, with $\overrightarrow{OM}$ the position vector of a material point in the coordinate system $\{\boldsymbol{e}_1', \boldsymbol{e}_2'\}$ related to the camera. For recentred ellipses, the shifting center $(x_{1_0}^I, x_{2_0}^I)$ was retrieved from each point on the measured deformed ellipse.

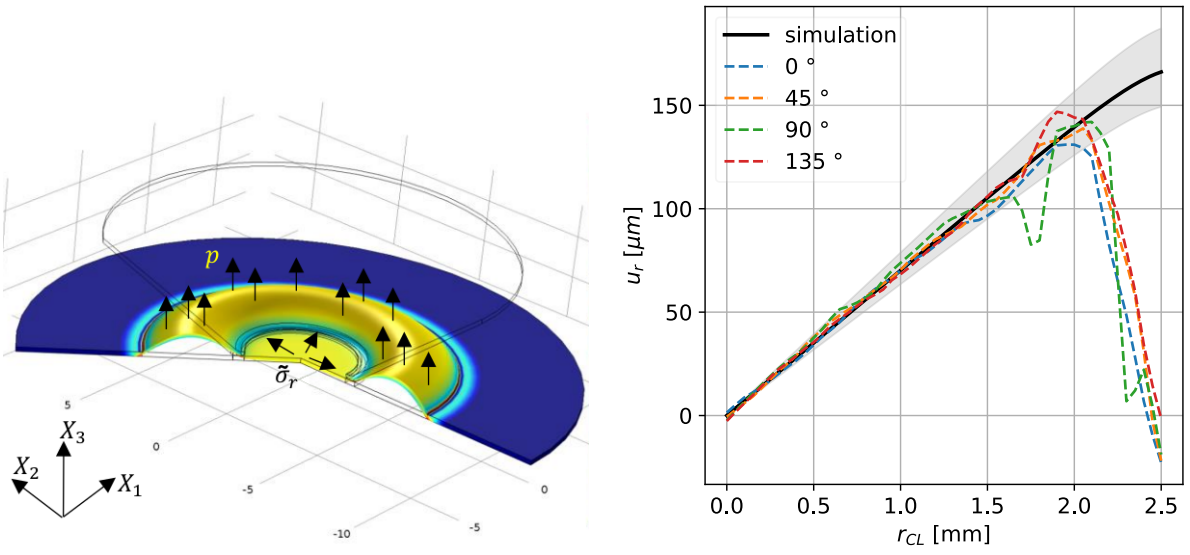

(a) **(b)**

Figure 13: (a) Deformed configuration of a 2D axisymmetric model subjected to a multi-axial ring suction test. (b) Comparison of radial displacement obtained with the FE model and the CutiScan. The filled grey area corresponds to 95% confidence interval of radial displacement obtained with the range $E_{\text{latex}} = 2.7 \pm 0.42$ MPa.

via Eq. (10) as $E_{\text{latex}} = 2.7$ MPa.

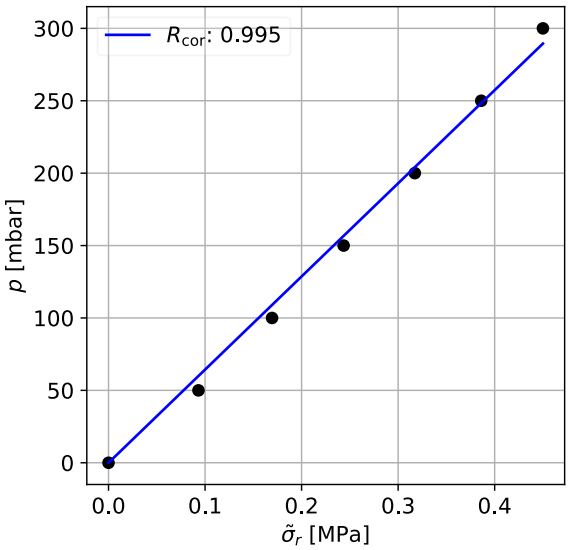

Figure 14: Correlation between the suction pressure p and the radial stress σ_r, with the slope $\xi = 633$.

3.2.2 Application to human forearm

Analogically, the application of our methodology to the data from a human forearm introduction in Section 2.1.4 is presented in this part. The mechanical response consists of displacement vectors (Fig. 15) and their relative radial component evaluated on circles and radial cutlines (Fig. 16).

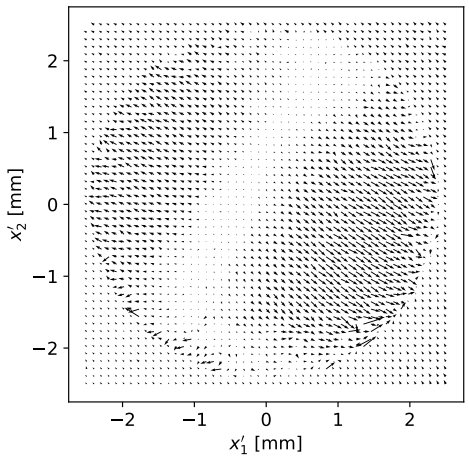

Figure 15: Displacement vector field for test 1 evaluated at the quasi-static state on DIC nodes for $p = 300$ mbar.

The parameter identification was performed on the 1 mm radius circle to avoid edge effects. As an example, the best-fit solution for the data set of the test 1 is shown in Fig. 17, for a converging parameter, set $\tilde{\boldsymbol{m}}_g^{(1)} = \{a = 1.0029 \text{ mm}; b = 1.0632 \text{ mm}; \phi = 60.24°; x_{10} = -17.8 \text{ µm}; x_{20} = 14.9 \text{ µm}\}$ with $R_{\text{cor}} = 0.9849$. The latter was juxtaposed with a simulation-based study carried out for the thickness $th_{\text{h}} = 1.47$ mm and for different elastic modulus values to calibrate the coefficients $\xi = 24300$ and $\eta = 1.03$. By applying Eq. (10) (where $\sigma_r = 0.0123$ MPa), Young's moduli along and across Langer's line are $E_1^{(1)} = 2.42 \pm 0.38$ MPa and $E_2^{(1)} = 0.188 \pm 0.002$ MPa, respectively.

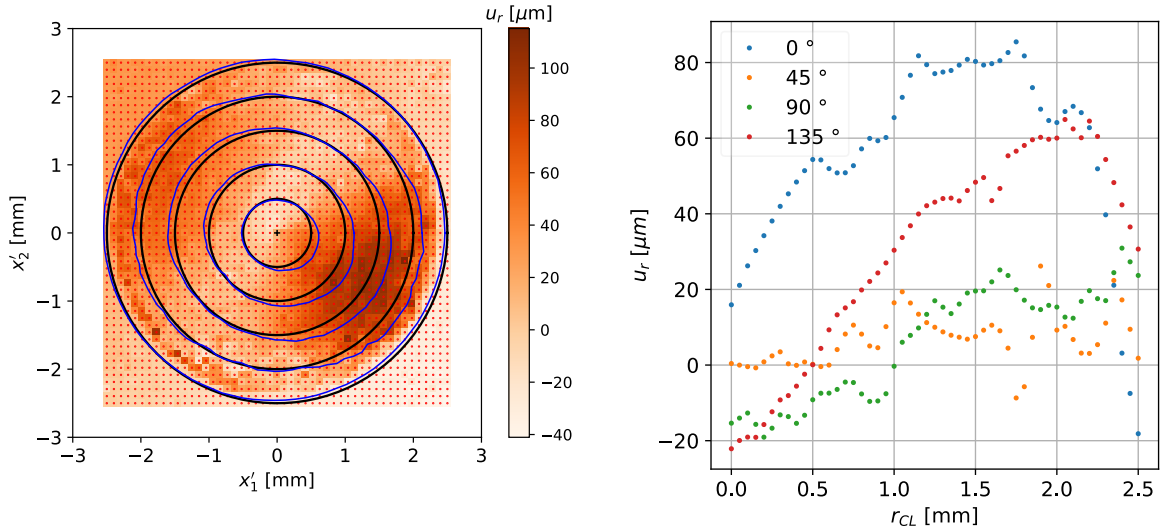

(a) Circles

(b) Radial cutlines

Figure 16: Mechanical response of the forearm skin subjected to multi-axial ring suction load. In (16a), the deformation is scaled by a factor of 2.

Skin material is known to exhibit a non-linear stress-strain curve; therefore, Eq. (6) can be applied only under a certain restriction: the correspondence between the incremental stress $d\sigma$ and strain $d\varepsilon$ is described by an elastic constant [22]. In other words, the applied stresses and their respective strains must have linear dependence, which can occur within the first and second linear regimes. However, in a non-unidirectional stretch, the slope $d\sigma/d\varepsilon = cte$ does not represent the real value of the elastic moduli E_1 and E_2 but ensures their constancy. In our case, the stress-strain curve for pressures between 100 and 500 mbar revealed that the elastic behavior is associated with the second linear regime, where the collagen fiber bundles are no longer crimped.

The identification results of $\tilde{\boldsymbol{m}}_g$ for all tests are listed in Table 1. Once outliers had been discarded based on the interquartile range [93], the resulting material parameters were similarly calculated (Fig. 18). Subsequently, $\hat{\phi} = 40.9 \pm 8.2°$. Using the formula (15), we obtained $\hat{E}_1 = 1.35 \pm 0.65$ MPa, and $\hat{E}_2 = 0.43 \pm 0.07$ MPa. Through Eq., we obtained $\tilde{\Delta}_{E_1} = 0.86$ MPa and $\tilde{\Delta}_{E_2} = 0.03$ MPa.

4 Discussion

The solutions of the static problem (1) given the boundary conditions on $\partial\Omega_D$ and $\partial\Omega_N$ were calculated numerically and analytically for numerous sets of material parameters (Section 3.1). Fig. 8 shows that the analytical solutions fit the FE data for a given parameter set. Similar results were obtained for the other parameter sets. Therefore, the proposed analytical model (6) has been validated in an unclassical approach. One of its relevant benefits is its application as a forward solver in stochastic optimization algorithms requiring thousands of computations, such as the Bayesian calibration [94, 95].

In Section 3.2.1, the model parameters of two soft materials were identified using an inverse solver using the Newton-Raphson algorithm. A sheet of homogeneous latex material was analyzed in the context of a calibration study to verify the developed framework's capability to accurately characterize the mechanical behavior of soft tissue with data issued from the CutiScan® apparatus. Figs. 11a and 11b demonstrate the material's isotropy and linear elasticity spatial linearity behaviors but within a limited area. Indeed, the displacement data captured between the circles of $r = 1.3$ mm and $r = 2$ mm (zone

Table 1: Numerical results of the inverse identification of $\tilde{\boldsymbol{m}}_g$. The initial parameter values were fixed to be $\{\phi = 45°; x_{10} = 0 \text{ mm}; x_{20} = 0 \text{ mm}\}$, whereas a and b are chosen according to the circle used for identification such that $a < b$. In our case, for $r = 1$ mm, we choose $a = 1$ mm and $b = 1.01$ mm. The best-fit curves of the 6 first test are available in Appendix A.2

.

Test	a (mm)	b (mm)	$\phi(°)$	$x_{10}(\mu\text{m})$	$x_{20}(\mu\text{m})$	R_{cor}
1	1.0029	1.0632	60.24	−17.80	14.9	0.9849
2	0.9990	1.0072	72.21	−8.3	1.7	0.9424
3	0.9992	1.0290	30.77	−4.7	−2.7	0.9687
4	1.0028	1.0306	27.61	−2.6	3.0	0.9685
5	1.0035	1.0282	31.25	−3	−8.0	0.9578
6	1.0020	1.0221	50.26	−2.7	18.9	0.9813
7	1.0039	1.0337	33.41	1.3	5.8	0.9774
8	1.0078	1.0381	43.09	−1.0	9.5	0.9868
9	1.0041	1.0301	42.35	−0.9	8.4	0.9774
10	1.0039	1.0485	36.95	−6.3	21.5	0.9889
11	1.0073	1.0321	50.80	−8.1	9.2	0.9648
12	1.0061	1.0363	46.39	2.3	13.4	0.9585
13	0.9948	1.0230	40.82	4.6	0.7	0.9826
14	1.0024	1.0265	26.25	−8.7	8.5	0.9834
15	1.0004	1.0316	37.36	−1.5	−19.5	0.9865
16	1.0058	1.0337	40.65	−6.9	6.5	0.9710
17	0.9991	1.0289	42.15	−4.0	0.3	0.9696
18	1.0063	1.0327	64.82	−9.4	−13.3	0.9866
19	1.0002	1.0260	28.81	6.0	7.0	0.9730
20	0.9960	1.0255	48.23	−1.7	17.0	0.9887
21	1.0017	1.0323	43.45	−11.7	6.7	0.9727
22	1.0002	1.0266	30.70	−1.3	12.1	0.9700
23	1.0024	1.0165	42.41	−1.9	−20.4	0.9902
24	0.9975	1.0266	49.16	3.0	3.4	0.9751
25	1.0077	1.0408	49.72	6.3	−13.0	0.9820
26	1.0039	1.0287	45.48	−2.2	−20.9	0.9786
27	1.0007	1.0201	43.09	5.4	−5.6	0.9660
28	0.9960	1.0368	46.48	12.9	−0.1	0.9861
29	0.9986	1.0175	63.46	6.7	7.5	0.9487
30	1.0024	1.0376	36.34	−0.2	8.6	0.9746

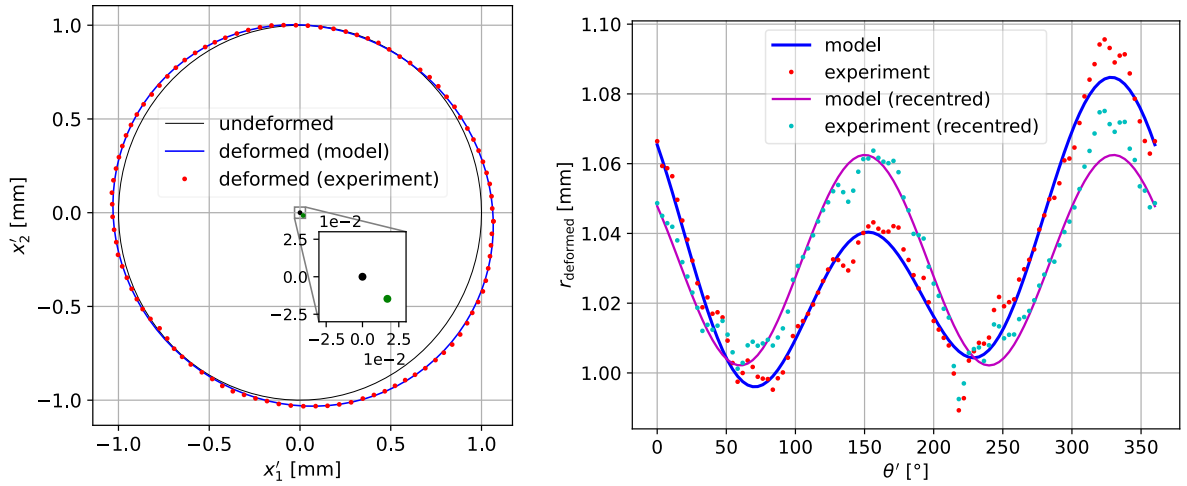

(a) **(b)**

Figure 17: (a) Model fitting with the identified parameters of the skin on the day 1, $\tilde{\boldsymbol{m}}_g^{(1)}$. The center position shifted from the black to the green dot. (b) Radius change r_{deformed} of the deformed ellipse before and after removing the rigid body motion (recentring). More details are available in Fig. 12.

Z_a) are highly perturbed. While between $r = 2$ mm and $r = 2.5$ mm (zone Z_b), the displacements decrease drastically until they reach 0 mm. This edge effect occurs because the material slips under the observable limit during the ring suction process. The disappearing zone is then interpreted as zero displacements with the DIC reader. This abnormality spreads toward the center and impacts the data in zones Z_a and Z_b.

If the multi-axis ring suction experiment was somehow identical to Laiacona et al.'s [24], the analysis approaches were quite different. the anisotropy angle is determined by fitting a deformed-and-rotated circle instead of fitting the radial strain, and the directional variations in Poisson's ratio were considered. In the given study, the data subjected to model optimization are gathered on a circle of radius $r = 1$ mm. The consistency of the mechanical response within the circular zone $r < 1.3$ mm and the deterministic nature of the inverse problem justify the choice of data quality over quantity. However, it is not recommended to select data near the center $r < 0.5$, where the experimental uncertainty Δ_{exp} is not neglected with respect to small displacements.

Identifying the offset rigid body motion parameters, $\{x_{10}, x_{20}\}$ is of major concern. The consequence of the offset is exhibited in Fig. 12, where the model and experimental data expressed with respect to the new origin are seemingly isotropic. The relative positions of the identified center shift are of the order of magnitude of the displacements. Thus, they cannot be neglected. Two technical reasons may describe the necessity of recentering. First, the origin of the DIC grid was fixed such that the width matches the diameter of the observable zone of the CutiScan® probe (Fig. 3). The real center of the deformed skin is then flexible. Second, even though the pressure is uniformly applied around the observable zone, many factors may lead to imperfect load distribution. Among them are the curvature of the forearm and the non-perpendicularity of the probe. In the latter situation, the device is not perfectly tangent to the skin surface.

A simulation FE model was developed in COMSOL Multiphysics® software to support the calibration study, where the ring suction experiment was modeled in a 2D axisymmetric geometry with a frictionless contact between the probe and the material surface (Figs. 13a and 19). The elastic modulus assigned

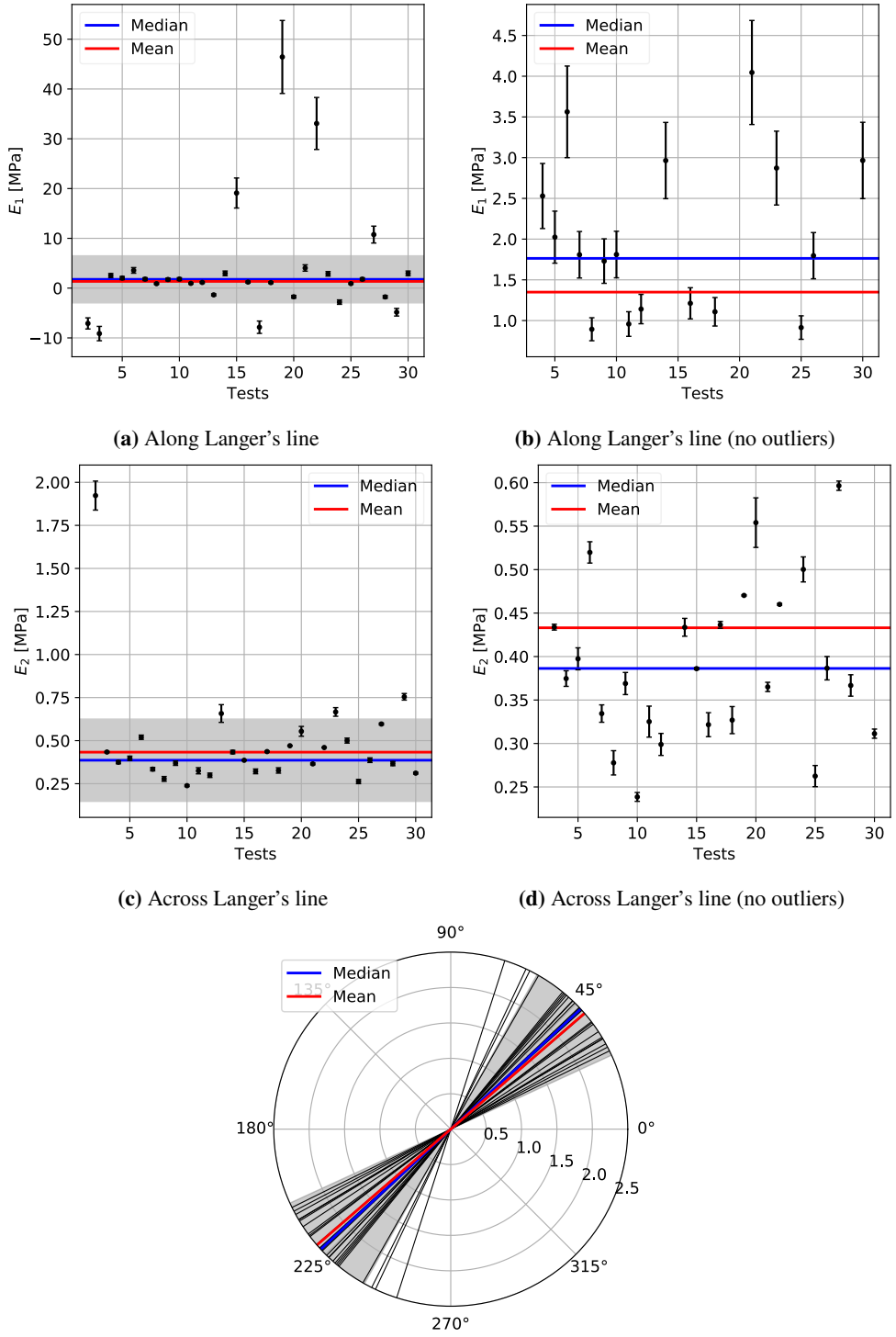

(a) Along Langer's line

(b) Along Langer's line (no outliers)

(c) Across Langer's line

(d) Across Langer's line (no outliers)

(e) Anisotropy angle ϕ

Figure 18: Illustration of the skin material parameters E_1 (a), E_2(c), and ϕ (e) for every test deducted from Table 1 and Eq. (10). Based on the interquartile range (IQR) method, the positive values inside the grey stripe are selected for calculating the dad-to-day deviation in (b) and (d). IQR is the interval [median - 1.5×IQ, median + 1.5×IQ], such that IQ is the difference between the 3rd and the 1st quartiles. The median was computed regarding all tests, while the mean was computed after discarding the outliers.

to the material was identified from a parallel uni-axial tensile test according to 3 directions with $E_{\text{latex}} = 2.7 \pm 0.4$ MPa. In the first step, the simulation was validated by comparing the calculated displacements along 4 directions of the deformed latex rubber *versus* the experimental data, which can be observed in Fig. 13b. A series of computations were performed for different negative pressure p values, where the radial stress in the observable zone was evaluated in post-treatment. Therefore, a linear correlation between p and σ_r was noticed, which validates the third hypothesis formulated in Section 2.2.1. Such a result would help simplify the full configuration into a radial stretch since the stress can be deduced directly from the applied pressure (Fig. 6a). Calibrating only the slope, ξ, would not be enough to evaluate the elastic moduli accurately. We introduced a corrective coefficient to compensate for the discrepancy resulting from the transition from a 2D axisymmetric to a plane model. We recommend that values ξ and η should be calibrated according to the material's thickness and stiffness by virtue of the simulation.

Once the methodology had been explored and verified based on the latex material, it was applied to 30 series of data acquired from the multi-axial ring suction test (CutiScan®) conducted on the forearm of one patient. Figs. 15, 16a, and 16b show that the human skin behaves as anisotropic material with two principal directions neighboring 45° and 135°, and that the validation limit of the spatial linearity is around $r = 1$ mm. Directions 0° and 90° with mostly identical mechanical responses indicate that the angle between the two principal axes is about 90°. The material is intended to be orthotropic. Since collagen fibers are stiffer than the ground substance, their axis of minimum, respectively maximum displacement is aligned along Langer's line, respectively across Langer's line [11, 13, 22, 30, 37]. Therefore, the Langer's line on the studied subject is oriented obliquely at a mean angle $\hat{\phi} = 40.9 \pm 8.2°$ relative to the forearm axis (Fig. 17). This result is in accordance with the literature [17, 71, 96, 97] but sensibly different from Khatyr *et al.* [13] (0–10°) . If the symmetry is admitted in the contralateral study on the right forearm, our result is similar to one reported by Lakhani *et al.* [67] and Kirby *et al.* [65]. Nevertheless, most recent studies, including ours, described efficient tools and methodology to determine the Langer's line orientation, historically defined on the forearm to be parallel to the forearm's long axis of the forearm [52, 53, 98].

The model parameters were identified with MARSAC for every test to investigate day-to-day variation material parameters and explore the proposed method's sensitivity (Table 1). The values of the correlation coefficient witness an accurate model fit for 28 tests ($R_{\text{cor}} > 0.95$). The parameters were retrieved from $\bar{\boldsymbol{m}}_g$ through Eq. (10) and have been projected in Fig. 18 for better visualization. As a result, Young's moduli along and across Langer's line are, respectively, $\hat{E}_1 = 1.35 \pm 0.65$ MPa and $\hat{E}_2 = 0.43 \pm 0.07$ MPa. The plots reveal that the deviations on $\hat{\phi}$, $\hat{\Delta}_\phi = 8.2°$, and on $\hat{E}_2$, $\hat{\Delta}_{E_2} = 0.07$ MPa, whose removed outliers were no more than 4, are relatively low, unlike $\hat{E}_1$ ($\hat{\Delta}_{E_1} = 0.65$ MPa), whose 12 outliers were discarded, as occurring in one of the two following situations: (i) u_1 is almost zero along Langer's line, and thus E_1 reaches higher stiffness, (ii) E_1 takes a negative value. In the latter scenario, negative E_1 indicates that the skin is compressed along Langer's line instead of being stretched. A dome inside the observable zone takes shape by pressing the probe strongly against the skin, and the mechanical response becomes unpredictable. The high sensitivity of E_1 assessment can be related to the fact that u_1 values are within the measurement uncertainty evaluated earlier in Section 3.2.1, $\Delta_{\text{exp}} = 2.7$ µm. On the other hand, the displacement u_2 across the higher stiffness direction is substantial compared to Δ_{exp}, which may justify the reliability of its assessment. As for ϕ, completely dissociated with E_1 and E_2, regarding the deviation $\hat{\Delta}_\phi = 8.2°$, the process of its identification can be considered robust.

To elucidate the variability of the material parameters from one day to another, we display in Ap-

pendix A.3 a series of skin pictures recorded at the first 6 tests. A change in the topography of the skin surface was visually noticed. A correlation between the skin lines' main direction and the anisotropy axis may appear. If we look at the tests $\{3, 4, 5, 6\}$, the furrows are mostly oriented along the same Langer's line identified in Table 1 with the respective angles $30.77°$, $27.61°$, $31.25°$, and $50.26°$, but not on test 1 with $\phi = 60.24°$. This result confirms the observations made in [96, 99]. Nevertheless, the correlation cannot be established on test 2, witnessing an absence of skin lines, and the relative ϕ is the most extreme with respect to the median. The skin microrelief network may depend on hydration conditions: the wrinkles are more pronounced in a dry stratum corneum [100]. The experimental protocol should consider particular attention to skin hydration to reduce the fluctuations of the material parameters, for instance, avoiding exposing the studied site to any liquid. Despite that, the day-to-day variation of skin wrinkles observed in Appendix A.3 could be associated with the change in the anisotropy axis. Considering that the uppermost layer's deformation is directly correlated to the radial stretch, any change in its texture would have an impact on the radial displacement distribution, and thus on ϕ. As for the rigid body motion, the identified values of x_{10} and x_{20} in Table 1 witness randomness over the 30 tests. Two causes can be suggested for this center shifting: the probe alignment with the skin surface and the friction between them. For the former, a manual setup of tangential contact would definitely be imperfect, and the skin slippage under the probe could not be uniform. As for the latter, a thorough tribology investigation is suggested to study the friction's effect on the center shifting. Regarding the recent observations in our experiments, we recommend carrying out the multi-axial ring suction test enclosed by a strictly standardized protocol. The protocol would include the following steps, reproducing the hydration conditions (*e.g.*, drying the measured site many hours before the test to ensure the appearance of the furrows), and holding the probe in a perfect perpendicular position to the skin surface with zero-load contact.

Since the value of the parameter $\nu_{12} = 0.43 \pm 0.09$ were fixed, based on the literature, the impact of its uncertainty on the identification accuracy had been studied. By averaging the standard deviations of the calibrated E_1 and E_2 for each test, we determined $\tilde{\Delta}_{E_1} = 0.86$ MPa and $\tilde{\Delta}_{E_2} = 0.03$ MPa. By comparing the uncertainties and the average values, one could notice that a 21% change in ν_{12} with regard to the displacement occurs in a change of 26% in E_1 and 3% in E_2. The uncertainty on E_2 is weakly correlated to ν_{12} because of the predominant displacement u_2 against u_1. However, as u_1 is low, E_1 is highly affected by $\Delta_{\nu_{12}}$. It is greatly suggested that particular attention must be given to the precision of ν_{12} measurement. To do this, a uni-axial test should be performed along the anisotropy axis ϕ identified by the MARSAC method.

Two topics regarding the material parameters are addressed hereby, their comparison to the previous studies in the literature and their physical interpretation. The ratio $\hat{E}_1/\hat{E}_2 = 3.14 \pm 1.60$ is conform to the results in [8, 11, 13, 16, 17, 98]. However, $\hat{E}_1 = 1.35 \pm 0.65$ MPa and $\hat{E}_2 = 0.43 \pm 0.07$ MPa are in good agreement with Young's modulus in some of the earlier cited papers [8, 13] but higher compared to [16, 17]. This latter behavior may occur when the effect of the epidermis layer (known to be stiffer than the dermis [40, 48, 101]) on the mechanical response is not neglected. This assumption is adequate with the CutiScan® device's function, which applies out-plane suction to cause an in-plane stretch in the superficial layers. Although the epidermis under superficial stretch dominates the skin stiffness, the dermis has a major effect on the mechanical response because the collagen and elastin fibers are present in the dermis, not in the epidermis. As an attempt to associate the material parameters with the micro-structure components, we state the following. Along Langer's line, E_1 describes the stiffness of the combination epidermis-collagen. While across Langer's line, E_2 describes the stiffness of the

combination epidermis-elastin. On the bright side, the anisotropy direction angle ϕ is insensitive to skin stiffness and purely driven by collagen's highest distribution angle.

5 Conclusions

MARSAC, an open-source framework coded in Python language, was built to characterize the anisotropic mechanical behavior of soft tissues. From an output video file gathered with the CutiScan® device during a ring suction test, MARSAC computes the displacement field using DIC and identifies the Langer's line direction ϕ, as well as the elastic moduli E_1 and E_2, along and across Langer's line, for a given Poisson's ratio value. An analytical orthotropic linear model was built and used to solve the displacement for applied pressure. In the first instance, the pipeline was applied to a homogeneous latex material as a verification and calibration step. Then, it was applied to public data consisting in a series of 30 multi-axial ring suction tests, at pressure $p = 300$ mbar, performed on a forearm of a 28-year-old Caucasian subject. The identification of Langer's line, $\hat{\phi} = 40.9 \pm 8.2\,^\circ$, interpreted as collagen fiber preferred direction, and the anisotropy ratio, $\hat{E_2}/\hat{E_1} = 3.14 \pm 1.60$, were in good agreement with the literature. The presented method showed a precise assessment of ϕ and E_2, but not E_1. The measured displacement along the stiffest direction is most of the time smaller than measurement error $\Delta_{\text{exp}} = 2.7$ µm; hence E_1 is less reliable. To conclude, the developed numerical method combined with the CutiScan® is a fast and accurate means to determine Langer's line locally in small areas. It would help the experimentalists efficiently use the commercial tool whose associated original software showed a lack of reliability [78]. The presented methodology will be applied to analyze clinical trial data of 30 volunteers to study the inter-subject variability. Also, It will also be integrated into a bi-material characterization software [45] to enhance its accuracy by adding the anisotropy aspect to the healthy skin around the abnormal scar.

Acknowledgments

The authors acknowledge the financial support of Region de Bourgogne Franche-Comté, France (grants n° 2018-Y-07543), the Luxembourg National Research Fund (OTP S-STR-8001-00-B), and French Agence Nationale de Recherche (ANR) grant (No. ANR-21-CE45-0025: `https://anr.fr/Project-ANR-21-CE45-0025`) for the project "(S-KELOID) Understanding Keloid Disorders: A multi-scale in vitro/in vivo/in silico approach towards digital twins of skin organoids on the chip". They thank Tiguida Kadiakhe for her help with the experiments.

A Appendix

A.1 Calibration study: Simulation model

A FE model was constructed in COMSOL Multiphysics® that simulates the multi-axial annular suction test. It was used to validate and calibrate the radial stress in the othrotopic linear elastic model (Eq. (6)) for assessing accurate values of the elastic moduli. In this 2D axisymmetric problem a thickness of 0.22 mm, the linear material elastic was adopted with Young's modulus $E = 2.7$ MPa and Poisson's ratio $\nu = 0.495$. The boundary conditions are described in Fig. 19.

A.2 Model fitting

See Fig. 20.

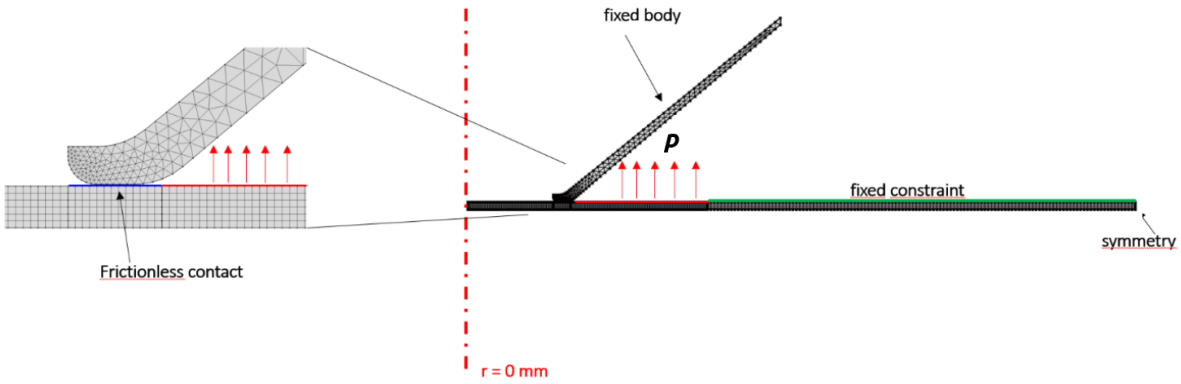

Figure 19: 2D axisymmetric model boundary conditions.

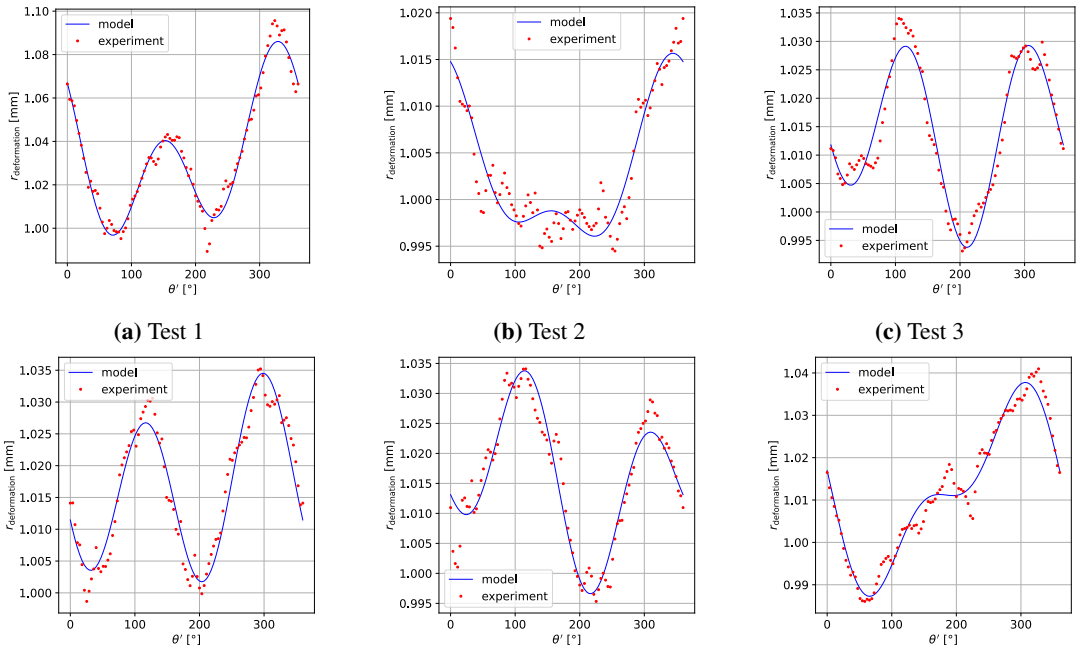

(a) Test 1 **(b)** Test 2 **(c)** Test 3

(d) Test 4 **(e)** Test 5 **(f)** Test 6

Figure 20: Model fitting along the circle of 1 mm radius for some tests.

A.3 Test snapshots

See Fig. 21.

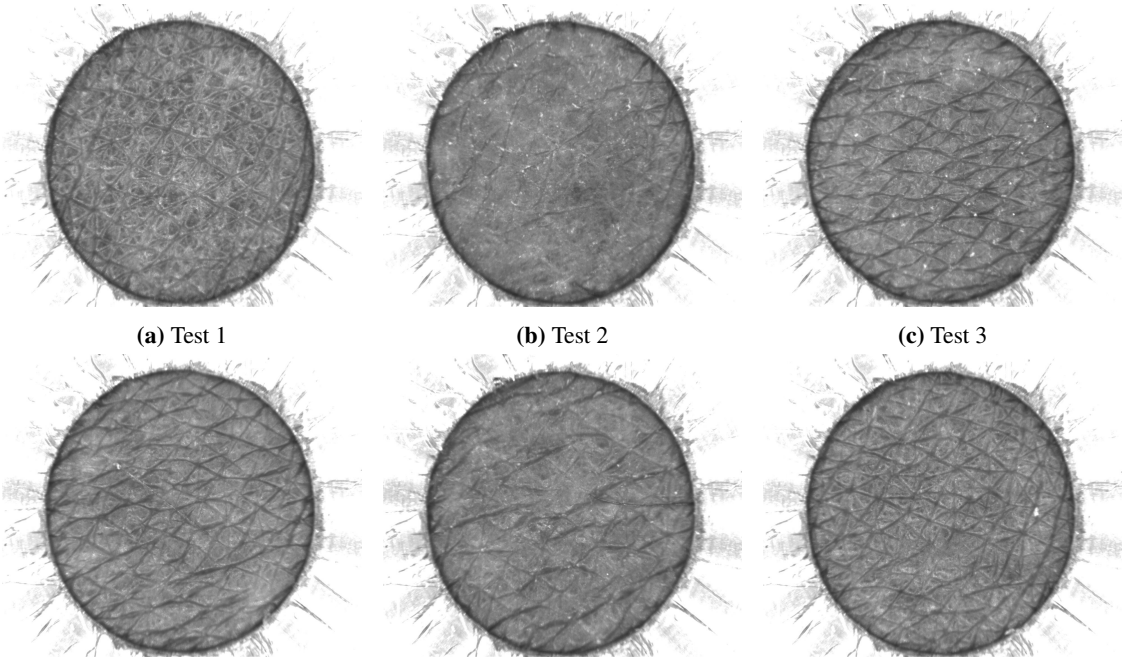

(a) Test 1 **(b)** Test 2 **(c)** Test 3

(d) Test 4 **(e)** Test 5 **(f)** Test 6

Figure 21: Skin texture snapshots for some tests.

References

[1] D. T. Corr and D. A. Hart, "Biomechanics of scar tissue and uninjured skin," *Advances in Wound Care*, vol. 2, no. 2, pp. 37–43, 2013.

[2] A. Buganza Tepole and E. Kuhl, "Systems-based approaches toward wound healing," *Pediatric Research*, vol. 73, no. 2, pp. 553–563, 2013.

[3] G. F. Odland and I. Goldsmith, "Physiology, biochemistry and molecular biology of the skin," *Oxford: Oxford University Press, 1991, Vol. I, p. 3*, 1991.

[4] C. Y. Tan, B. Statham, R. Marks, and P. A. Payne, "Skin thickness measurement by pulsed ultrasound; its reproducibility, validation and variability," *British Journal of Dermatology*, vol. 106, no. 6, pp. 657–667, 1982.

[5] H. Oxlund, J. Manschot, and A. Viidik, "The role of elastin in the mechanical properties of skin," *Journal of Biomechanics*, vol. 21, no. 3, pp. 213–218, 1988.

[6] J. Burton and W. Cunliffe, *Subcutaneous Fat: text book of dermatology*. Blackwell Scientific Publications, New York, 1992.

[7] W. A. Sodeman and G. E. Burch, "A direct method for the estimation of skin distensibility with its application to the study of vascular states," *The Journal of Clinical Investigation*, vol. 17, no. 6, pp. 785–793, 1938.

[8] P. Wijn, A. Brakkee, G. Stienen, and A. Vendrik, "Mechanical properties of the human skin in vivo for small deformations; a comparison of uniaxial strain and torsion measurements," in *Bed sore biomechanics*, pp. 103–108, Springer, 1976.

[9] T. Burlin, W. Hutton, and H. Ranu, "A method of in vivo measurement of the elastic properties of skin in radiotherapy patients," *Journal of Investigative Dermatology*, vol. 69, no. 3, 1977.

[10] J. F. M. Manschot and A. Brakkee, "The measurement and modelling of the mechanical properties of human skin in vivo—i. the measurement," *Journal of Biomechanics*, vol. 19, no. 7, pp. 511–515, 1986.

[11] J. Manschot and A. Brakkee, "The measurement and modelling of the mechanical properties of human skin in vivo—ii. the model," *Journal of Biomechanics*, vol. 19, no. 7, pp. 517–521, 1986.

[12] R. Meijer, L. F. A. Douven, and C. W. J. Oomens, "Characterisation of anisotropic and non-linear behaviour of human skin in vivo," *Computer Methods in Biomechanics and Biomedical Engineering*, vol. 2, no. 1, pp. 13–27, 1999.

[13] F. Khatyr, C. Imberdis, P. Vescovo, D. Varchon, and J.-M. Lagarde, "Model of the viscoelastic behaviour of skin in vivo and study of anisotropy," *Skin Research and Technology*, vol. 10, no. 2, pp. 96–103, 2004.

[14] E. Jacquet, G. Josse, F. Khatyr, and C. Garcin, "A new experimental method for measuring skin's natural tension," *Skin Research and Technology*, vol. 14, no. 1, pp. 1–7, 2008.

[15] S. L. Evans and C. A. Holt, "Measuring the mechanical properties of human skin in vivo using digital image correlation and finite element modelling," *The Journal of Strain Analysis for Engineering Design*, vol. 44, no. 5, pp. 337–345, 2009.

[16] C. Flynn, A. Taberner, and P. Nielsen, "Mechanical characterisation of in vivo human skin using a 3d force-sensitive micro-robot and finite element analysis," *Biomechanics and Modeling in Mechanobiology*, vol. 10, no. 1, pp. 27–38, 2011.

[17] G. Boyer, J. Molimard, M. B. Tkaya, H. Zahouani, M. Pericoi, and S. Avril, "Assessment of the in-plane biomechanical properties of human skin using a finite element model updating approach combined with an optical full-field measurement on a new tensile device," *Journal of the Mechanical Behavior of Biomedical Materials*, vol. 27, pp. 273–282, 2013.

[18] E. Jacquet, S. Joly, J. Chambert, K. Rekik, and P. Sandoz, "Ultra-light extensometer for the assessment of the mechanical properties of the human skin in vivo," *Skin Research and Technology*, vol. 23, no. 4, pp. 531–538, 2017.

[19] J. Chambert, T. Lihoreau, S. Joly, B. Chatelain, P. Sandoz, P. Humbert, E. Jacquet, and G. Rolin, "Multimodal investigation of a keloid scar by combining mechanical tests in vivo with diverse imaging techniques," *Journal of the Mechanical Behavior of Biomedical Materials*, vol. 99, pp. 206–215, 07 2019.

[20] W. A. Wa, "Biaxial tension test of human skin in vivo.," *Bio-Medical Materials and Engineering*, vol. 4, no. 7, pp. 473–486, 1994.

[21] H. Alexander and T. Cook, "Accounting for natural tension in the mechanical testing of human skin," *Journal of Investigative Dermatology*, vol. 69, no. 3, pp. 310–314, 1977.

[22] R. Reihsner, B. Balogh, and E. Menzel, "Two-dimensional elastic properties of human skin in terms of an incremental model at the in vivo configuration," *Medical Engineering & Physics*, vol. 17, no. 4, pp. 304–313, 1995.

[23] R. Reihsner and E. Menzel, "On the orthogonal anisotropy of human skin as a function of anatomical region," *Connective Tissue Research*, vol. 34, no. 2, pp. 145–160, 1996.

[24] D. Laiacona, J. Cohen, K. Coulon, Z. Lipsky, C. Maiorana, R. Boltyanskiy, E. Dufresne, and G. German, "Non-invasive in vivo quantification of human skin tension lines," *Acta Biomaterialia*, vol. 88, pp. 141–148, 2019.

[25] R. Grahame and P. Holt, "The influence of ageing on the in vivo elasticity of human skin," *Gerontology*, vol. 15, no. 2-3, pp. 121–139, 1969.

[26] P. Elsner, A. Barel, E. Berardesca, B. Gabard, and J. Serup, "Mechanical function of the skin: state of the art," *Skin Bioengineering: Techniques and Applications in Dermatology and Cosmetology*, vol. 26, pp. 69–83, 1998.

[27] S. Diridollou, F. Patat, F. Gens, L. Vaillant, D. Black, J. Lagarde, Y. Gall, and M. Berson, "In vivo model of the mechanical properties of the human skin under suction," *Skin Research and Technology*, vol. 6, no. 4, pp. 214–221, 2000.

[28] F. Hendriks, D. v. Brokken, J. Van Eemeren, C. Oomens, F. Baaijens, and J. Horsten, "A numerical-experimental method to characterize the non-linear mechanical behaviour of human skin," *Skin Research and Technology*, vol. 9, no. 3, pp. 274–283, 2003.

[29] A. O. Barel, W. Courage, and P. Clarys, "Suction chamber method for measurement of skin mechanics: The new digital version of the cutometer," in *Handbook of Non-Invasive Methods and the Skin*, pp. 583–591, CRC press, 2006.

[30] A. Delalleau, G. Josse, J.-M. Lagarde, H. Zahouani, and J.-M. Bergheau, "A nonlinear elastic behavior to identify the mechanical parameters of human skin in vivo," *Skin Research and Technology*, vol. 14, no. 2, pp. 152–164, 2008.

[31] B. Müller, J. Elrod, M. Pensalfini, R. Hopf, O. Distler, C. Schiestl, and E. Mazza, "A novel ultra-light suction device for mechanical characterization of skin," *PLOS ONE*, vol. 13, pp. 1–22, 08 2018.

[32] D. Bader and P. Bowker, "Mechanical characteristics of skin and underlying tissues in vivo," *Biomaterials*, vol. 4, no. 4, pp. 305–308, 1983.

[33] Y. Zheng and A. F. Mak, "Effective elastic properties for lower limb soft tissues from manual indentation experiment," *IEEE Transactions on Rehabilitation Engineering*, vol. 7, no. 3, pp. 257–267, 1999.

[34] K. Khaothong, "In vivo measurements of the mechanical properties of human skin and muscle by inverse finite element method combined with the indentation test," in *6th World Congress of Biomechanics (WCB 2010). August 1-6, 2010 Singapore*, pp. 1467–1470, Springer, 2010.

[35] J. T. Iivarinen, R. K. Korhonen, P. Julkunen, and J. S. Jurvelin, "Experimental and computational analysis of soft tissue stiffness in forearm using a manual indentation device," *Medical Engineering & Physics*, vol. 33, no. 10, pp. 1245–1253, 2011.

[36] L. Zhou, S. Wang, J. Zhang, J. Wang, and C. Li, "In vivo measurement of the anisotropic mechanical properties of human skin by indentation test," *Mechanics of Materials*, vol. 158, p. 103851, 2021.

[37] R. Sanders, "Torsional elasticity of human skin in vivo," *Pflügers Archiv*, vol. 342, no. 3, pp. 255–260, 1973.

[38] P. G. Agache, C. Monneur, J. L. Lévêque, and J. De Rigal, "Mechanical properties and young's modulus of human skin in vivo," *Archives of Dermatological Research*, vol. 269, no. 3, pp. 221–232, 1980.

[39] C. Escoffier, J. De Rigal, A. Rochefort, R. Vasselet, J.-L. Lévêque, and P. G. Agache, "Age-related mechanical properties of human skin: an in vivo study," *Journal of Investigative Dermatology*, vol. 93, no. 3, pp. 353–357, 1989.

[40] P. Agache and P. Humbert, *Measuring the Skin*. Springer Science & Business Media, 2004.

[41] A. Kalra, A. Lowe, and A. Al-Jumaily, "Mechanical behaviour of skin: a review," *J. Mater. Sci. Eng*, vol. 5, no. 4, p. 1000254, 2016.

[42] H. Joodaki and M. B. Panzer, "Skin mechanical properties and modeling: A review," *Proceedings of the Institution of Mechanical Engineers, Part H: Journal of Engineering in Medicine*, vol. 232, no. 4, pp. 323–343, 2018.

[43] G. Limbert, "Mathematical and computational modelling of skin biophysics: a review," *Proceedings of the Royal Society A: Mathematical, Physical and Engineering Sciences*, vol. 473, no. 2203, p. 20170257, 2017.

[44] D. Sutula, A. Elouneg, M. Sensale, F. Chouly, J. Chambert, A. Lejeune, D. Baroli, P. Hauseux, S. Bordas, and E. Jacquet, "An open source pipeline for design of experiments for hyperelastic models of the skin with applications to keloids," *Journal of the Mechanical Behavior of Biomedical Materials*, vol. 112, p. 103999, 2020.

[45] A. Elouneg, D. Sutula, J. Chambert, A. Lejeune, S. Bordas, and E. Jacquet, "An open-source fenics-based framework for hyperelastic parameter estimation from noisy full-field data: Application to heterogeneous soft tissues," *Computers & Structures*, vol. 255, p. 106620, 2021.

[46] I. Yannas, "Principles of skin regeneration," in *Biomaterials for Treating Skin Loss* (D. Orgill and C. Blanco, eds.), Woodhead Publishing Series in Biomaterials, pp. 212–230, Woodhead Publishing, 2009.

[47] I. V. Yannas, *Tissue and Organ Regeneration in Adults: Extension of the Paradigm to Several Organs*. Springer New York, 2015.

[48] A. G. Ferdman and I. V. Yannas, "Scattering of light from histologic sections: a new method for the analysis of connective tissue," *Journal of Investigative Dermatology*, vol. 100, no. 5, pp. 710–716, 1993.

[49] F. Hendriks, "Mechanical behaviour of human skin in vivo-a literature review," in *Nat. Lab. Unclassified Report 820. Philips Research Laboratories*, Citeseer, 2001.

[50] C. Edwards and R. Marks, "Evaluation of biomechanical properties of human skin," *Clinics in Dermatology*, vol. 13, no. 4, pp. 375–380, 1995.

[51] B. Finlay, "Scanning electron microscopy of the human dermis under uni-axial strain," *Biomedical Engineering*, vol. 4, no. 7, pp. 322–327, 1969.

[52] K. Langer, "Zue anatomie und physiologie de haut. ueber der spaltbarkeit der cutis," *Sitzungsberich der Academie der Wissenschaften in Wien*, vol. 44, no. 19, p. 1861, 1861.

[53] K. Langer, "On the anatomy and physiology of the skin: I. the cleavability of the cutis," *British Journal of Plastic Surgery*, vol. 31, no. 1, pp. 3–8, 1978.

[54] M. Ridge and V. Wright, "The directional effects of skin: A bio-engineering study of skin with particular reference to Langer's lines," *Journal of Investigative Dermatology*, vol. 46, no. 4, pp. 341–346, 1966.

[55] T. Gibson, H. Stark, and J. Evans, "Directional variation in extensibility of human skin in vivo," *Journal of Biomechanics*, vol. 2, no. 2, pp. 201–204, 1969.

[56] J. B. Finlay, *Biodynamic studies of human skin: torsional characteristics in relation to structure*. PhD thesis, University of Strathclyde, 1970.

[57] X. Markenscoff and I. Yannas, "On the stress-strain relation for skin," *Journal of Biomechanics*, vol. 12, no. 2, pp. 127–129, 1979.

[58] A. N. Annaidh, K. Bruyère, M. Destrade, M. D. Gilchrist, and M. Otténio, "Characterization of the anisotropic mechanical properties of excised human skin," *Journal of the Mechanical Behavior of Biomedical Materials*, vol. 5, no. 1, pp. 139–148, 2012.

[59] A. Ní Annaidh, K. Bruyère, M. Destrade, M. D. Gilchrist, C. Maurini, M. Otténio, and G. Saccomandi, "Automated estimation of collagen fibre dispersion in the dermis and its contribution to the anisotropic behaviour of skin," *Annals of Biomedical Engineering*, vol. 40, no. 8, pp. 1666–1678, 2012.

[60] S. Aarabi, K. A. Bhatt, Y. Shi, J. Paterno, E. I. Chang, S. A. Loh, J. W. Holmes, M. T. Longaker, H. Yee, and G. C. Gurtner, "Mechanical load initiates hypertrophic scar formation through decreased cellular apoptosis," *The FASEB Journal*, vol. 21, no. 12, pp. 3250–3261, 2007.

[61] D. Son and A. Harijan, "Overview of surgical scar prevention and management," *Journal of Korean Medical Science*, vol. 29, no. 6, pp. 751–757, 2014.

[62] S. Nickell, M. Hermann, M. Essenpreis, T. J. Farrell, U. Krämer, and M. S. Patterson, "Anisotropy of light propagation in human skin," *Physics in Medicine and Biology*, vol. 45, pp. 2873–2886, sep 2000.

[63] S. Sakai, M. Yamanari, Y. Lim, N. Nakagawa, and Y. Yasuno, "In vivo evaluation of human skin anisotropy by polarization-sensitive optical coherence tomography," *Biomedical Optics Express*, vol. 2, pp. 2623–2631, Sep 2011.

[64] S. Gahagnon, Y. Mofid, G. Josse, and F. Ossant, "Skin anisotropy in vivo and initial natural stress effect: A quantitative study using high-frequency static elastography," *Journal of Biomechanics*, vol. 45, no. 16, pp. 2860–2865, 2012.

[65] M. A. Kirby, P. Tang, H.-C. Liou, M. Kuriakose, J. J. Pitre, T. N. Pham, R. E. Ettinger, R. K. Wang, M. O'Donnell, and I. Pelivanov, "Probing elastic anisotropy of human skin in vivo with light using non-contact acoustic micro-tapping oce and polarization sensitive oct," *Scientific reports*, vol. 12, no. 1, pp. 1–17, 2022.

[66] T. K. Tonge, L. S. Atlan, L. M. Voo, and T. D. Nguyen, "Full-field bulge test for planar anisotropic tissues: Part i – experimental methods applied to human skin tissue," *Acta Biomaterialia*, vol. 9, no. 4, pp. 5913–5925, 2013.

[67] P. Lakhani, K. Dwivedi, A. Parashar, and N. Kumar, "Non-invasive in vivo quantification of directional dependent variation in mechanical properties for human skin," *Frontiers in Bioengineering and Biotechnology*, vol. 9, p. 749492, 10 2021.

[68] H. Stark, "Directional variations in the extensibility of human skin," *British Journal of Plastic Surgery*, vol. 30, no. 2, pp. 105–114, 1977.

[69] Y. A. Kvistedal and P. M. F. Nielsen, "Estimating material parameters of human skin in vivo," *Biomechanics and Modeling in Mechanobiology*, vol. 8, pp. 1–8, Nov. 2007.

[70] P. D. Verhaegen, E. M. Res, A. Van Engelen, E. Middelkoop, and P. P. Van Zuijlen, "A reliable, non-invasive measurement tool for anisotropy in normal skin and scar tissue," *Skin Research and Technology*, vol. 16, no. 3, pp. 325–331, 2010.

[71] K. Rosicka, M. Hill, and M. Wdowski, "Skin anisotropy: Finding the optimal incision line for volar forearm in males and females," *Journal of the Mechanical Behavior of Biomedical Materials*, vol. 124, p. 104805, 2021.

[72] J. Serup, G. B. Jemec, and G. L. Grove, *Handbook of Non-Invasive Methods and the Skin*. CRC press, 2006.

[73] C. Rosado, F. Antunes, R. Barbosa, R. Fernando, and L. M. Rodrigues, "Cutiscan®-a new system of biomechanical evaluation of the skin in vivo-comparative study of use depending on the anatomical site," *Biomedical and Biopharmaceutical Research*, vol. 12, no. 1, pp. 49–57, 2015.

[74] C. Rosado, F. Antunes, R. Barbosa, R. Fernando, M. Estudante, H. N. Silva, and L. M. Rodrigues, "About the in vivo quantitation of skin anisotropy," *Skin Research and Technology*, vol. 23, no. 3, pp. 429–436, 2017.

[75] H. Silva, R. Francisco, and L. Rodrigues, "Texture analysis is a useful tool to characterize the cutaneous biomechanical profile: A análise de textura é uma ferramenta útil para caracterizar o perfil biomecânico cutâneo," *Journal Biomedical and Biopharmaceutical Research*, vol. 16, pp. 188–194, 12 2019.

[76] M. A. Kim, Y. C. Jung, and E. J. Kim, "Evaluation of anisotropic properties of striae distensae with regard to skin surface texture and viscoelasticity," *Skin Research and Technology*, vol. 26, no. 2, pp. 220–225, 2020.

[77] A. Elouneg, Q. Lucot, E. Veyrat-Durebex, A. Lejeune, J. Chambert, T. Lihoreau, B. Chatelain, G. Rolin, and E. Jacquet, "Biomechanical characterization of earlobe keloid by ring suction test," *Computer Methods in Biomechanics and Biomedical Engineering*, vol. 23, no. sup1, pp. S99–S100, 2020.

[78] M. Anthonissen, E. Van den Kerckhove, P. Moortgat, I. Geraerts, N. Devoogdt, T. De Vrieze, and A. De Groef, "Can the CutiScan CS 100® measure anisotropy and viscoelasticity in scar tissue after mastectomy? a reliability and validity study," *Skin Research and Technology*, vol. 28, no. 2, pp. 246–253, 2022.

[79] A. Elouneg, A. Bertin, Q. Lucot, V. Tissot, E. Jacquet, J. Chambert, and A. Lejeune, "In vivo skin anisotropy dataset from annular suction test," *Data in Brief*, vol. 40, p. 107835, 2022.

[80] A. Elouneg, A. Lejeune, E. Jacquet, J. Chambert, L. A. A. Beex, and S. Bordas, "Anisotropic mechanical characterization of human skin by in vivo multi-axial ring suction test." DOI: 10.6084/m9.figshare.19778506, May 2022.

[81] D. André, "PyDIC, a python suite for local digital image correlation." `https://gitlab.com/damien.andre/pydic` 2019. Accessed: 15 May 2022.

[82] B. D. Lucas and T. Kanade, "An iterative image registration technique with an application to stereo vision," in *Proc 7th Intl Joint Conf on Artificial Intelligence (IJCAI). August 24-28*, pp. 674–679, Vancouver, British Columbia, 1981.

[83] J. E. Solem, *Programming Computer Vision with Python: Tools and Algorithms for Analyzing Images*. " O'Reilly Media, Inc.", 2012.

[84] Y. Takema, Y. Yorimoto, M. Kawai, and G. Imokawa, "Age-related changes in the elastic properties and thickness of human facial skin," *British Journal of Dermatology*, vol. 131, no. 5, pp. 641–648, 1994.

[85] I. Doghri, *Mechanics of deformable solids: linear, nonlinear, analytical and computational aspects*. Springer-Verlag, Berlin, Heidelberg, 2000.

[86] R. M. Jones, *Mechanics of composite materials*. CRC Press, Boca Raton, 2nd ed., 2018.

[87] A. Logg, K.-A. Mardal, and G. Wells, *Automated solution of differential equations by the finite element method: The FEniCS book*, vol. 84. Springer Science & Business Media, 2012.

[88] T. C. T. Ting and T. Chen, "Poisson's ratio for anisotropic elastic materials can have no bounds," *The Quarterly Journal of Mechanics and Applied Mathematics*, vol. 58, pp. 73–82, 02 2005.

[89] C. Pailler-Mattei, S. Bec, and H. Zahouani, "In vivo measurements of the elastic mechanical properties of human skin by indentation tests," *Medical Engineering & Physics*, vol. 30, no. 5, pp. 599–606, 2008.

[90] A. Levy, M. B.-O. Frank, and A. Gefen, "The biomechanical efficacy of dressings in preventing heel ulcers," *Journal of Tissue Viability*, vol. 24, no. 1, pp. 1–11, 2015.

[91] M. Destrade, M. Gilchrist, J. Motherway, and J. Murphy, "Slight compressibility and sensitivity to changes in poisson's ratio," *International Journal for Numerical Methods in Engineering*, vol. 90, no. 4, pp. 403–411, 2012.

[92] K. K. Dwivedi, P. Lakhani, S. Kumar, and N. Kumar, "Effect of collagen fibre orientation on the poisson's ratio and stress relaxation of skin: an ex vivo and in vivo study," *Royal Society Open Science*, vol. 9, no. 3, p. 211301, 2022.

[93] F. M. Dekking, C. Kraaikamp, H. P. Lopuhaä, and L. E. Meester, *A Modern Introduction to Probability and Statistics: Understanding why and how*, vol. 488. Springer, 2005.

[94] M. Zeraatpisheh, S. P. Bordas, and L. A. Beex, "Bayesian model uncertainty quantification for hyperelastic soft tissue models," *Data-Centric Engineering*, vol. 2, p. e9, 2021.

[95] T. Han, T. Lee, J. Ledwon, E. Vaca, S. Turin, A. Kearney, A. K. Gosain, and A. B. Tepole, "Bayesian calibration of a computational model of tissue expansion based on a porcine animal model," *Acta Biomaterialia*, vol. 137, pp. 136–146, 2022.

[96] H. Zahouani, M. Djaghloul, R. Vargiolu, S. Mezghani, and M. E. L. Mansori, "Contribution of human skin topography to the characterization of dynamic skin tension during senescence: morpho-mechanical approach," *Journal of Physics: Conference Series*, vol. 483, p. 012012, mar 2014.

[97] J. Cha, J. Kim, and S. Kim, "Noninvasive determination of fiber orientation and tracking 2-dimensional deformation of human skin utilizing spatially resolved reflectance of infrared light measurement in vivo," *Measurement*, vol. 142, pp. 170–180, 2019.

[98] X. Liang and S. A. Boppart, "Biomechanical properties of in vivo human skin from dynamic optical coherence elastography," *IEEE Transactions on Biomedical Engineering*, vol. 57, no. 4, pp. 953–959, 2010.

[99] M. Ayadh, M.-A. Abellan, C. Helfenstein-Didier, A. Bigouret, and H. Zahouani, "Methods for characterizing the anisotropic behavior of the human skin's relief and its mechanical properties in vivo linked to age effects," *Surface Topography: Metrology and Properties*, vol. 8, p. 014002, mar 2020.

[100] G. Limbert and E. Kuhl, "On skin microrelief and the emergence of expression micro-wrinkles," *Soft matter*, vol. 14, no. 8, pp. 1292–1300, 2018.

[101] X. Feng, G.-Y. Li, A. Ramier, A. M. Eltony, and S.-H. Yun, "In vivo stiffness measurement of epidermis, dermis, and hypodermis using broadband rayleigh-wave optical coherence elastography," *Acta Biomaterialia*, 2022.